J. Fluid Mech. (2024), *vol*. 985, A46, doi:10.1017/jfm.2024.293

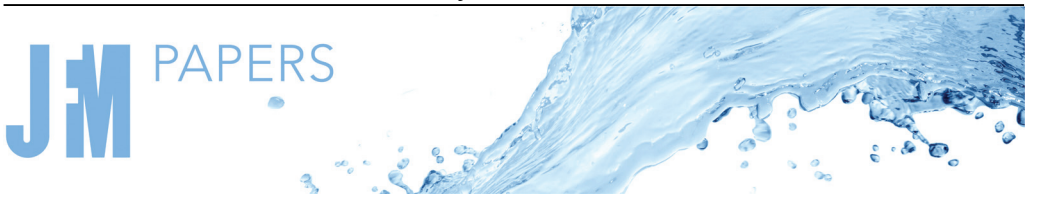

Integral methods for friction decomposition and their extensions to rough-wall flows

Wen Zhang[1,2], **Xiang I.A. Yang**[3,†], **Peng Chen**[1,2] **and Minping Wan**[1,2,†]

[1]Guangdong Provincial Key Laboratory of Turbulence Research and Applications, Department of Mechanics and Aerospace Engineering, Southern University of Science and Technology, Shenzhen 518055, PR China

[2]Guangdong-Hong Kong-Macao Joint Laboratory for Data-Driven Fluid Mechanics and Engineering Applications, Southern University of Science and Technology, Shenzhen 518055, PR China

[3]Mechanical Engineering, Pennsylvania State University, PA 16802, USA

(Received 8 September 2023; revised 6 March 2024; accepted 14 March 2024)

A primary objective of integral methods, such as the momentum integral method, is to discern the physical processes contributing to skin friction. These methods encompass the momentum, kinetic energy and angular momentum integrals. This paper reformulates existing integrals based on the double-averaged Navier–Stokes equations, and extends their application to flows over rough walls. Our derivation yields distinct decompositions for the bottom-wall viscous friction coefficient, denoted as C_S, and the roughness element drag coefficient C_R. The decompositions comprise three terms: a viscous term, a turbulent term and a roughness (dispersive) term – regardless of the flow configuration, be it channel or boundary layer. Notably, when these integrals are evaluated for laminar flow scenarios, only the viscous term remains significant. In addition, we elucidate the spatial distributions of the terms within these decompositions. To demonstrate the practicality of our formulations, we apply them to analyse data from direct numerical simulations of turbulent half-channel flows. These flows feature aligned and staggered cubical roughness at various packing densities. Our analyses, based on kinetic-energy-oriented decompositions, reveal that when the surface coverage density λ_p is small, the dominant terms within the decompositions are the viscous and turbulent terms. With increasing λ_p, the viscous dissipation term decreases, while the turbulent production term increases and then decreases. These variations arise from a subdued near-wall cycle and the development of a shear layer at the height of the cubes.

Key words: turbulent boundary layers

† Email addresses for correspondence: xzy48@psu.edu, wanmp@sustech.edu.cn

1. Motivation

Pioneered by Fukagata, Iwamoto & Kasagi (2002), integral methods and decompositions of skin friction have been employed by many as diagnostic tools in their data analyses. These analyses have subsequently led to new insights into the physical processes that contribute to the generation of skin friction. This paper explores alternative formulations of the existing integrals and decompositions for flows above smooth surfaces, and extensions of these integrals and decompositions for flows above rough surfaces. Considering the successes of the integral methods thus far (Fukagata, Iwamoto & Hasegawa 2024), extending the existing methods to previously unexplored flow scenarios promises new insights, and such endeavours should need no further motivation. This is particularly true for rough-wall boundary layers, which are common in fluid engineering (Jiménez 2004; Flack & Schultz 2010; Chung *et al.* 2021). In this first section, we discuss two considerations that motivate the exploration of alternative integrals for smooth walls and the need for new formulations for rough walls. In §§ 2 and 3, we will summarize the equations and review prior integral methods in greater detail.

The first consideration involves distinguishing between effects that are internal and external to the flow. A theory may focus exclusively on effects that are internal or external. As an illustrative example, we examine Kármán's integral (Schlichting & Gersten 2017). The integral reads

$$\frac{\tau_w}{\rho U_r^2} = \frac{1}{U_r^2}\frac{\partial}{\partial t}(U_r\delta_1) + \frac{\partial \delta_2}{\partial x_1} + \frac{2\delta_2+\delta_1}{U_r}\frac{\partial U_r}{\partial x_1} + \frac{v_w}{U_r}. \tag{1.1}$$

Here, τ_w is the wall shear stress, U_r is a reference velocity, δ_1 and δ_2 are the displacement and momentum thickness height, v_w is the blowing/suction velocity at the wall, and x_1 is the streamwise coordinate. The equation gives the force balance. It focuses on processes that are external to the boundary layer: given a control volume, the terms on the right-hand side represent external momentum fluxes to the boundary layer. Notice that their values depend on the frame of reference. Equation (1.1) is formally a decomposition of the skin friction. However, such decomposition provides little information on the processes that contribute to the generation of skin friction – terms such as the Reynolds shear stress that represents the effect of turbulence are absent.

We now turn to the integral methods. Here, we take the momentum integral in Fukagata *et al.* (2002) as an illustrative example. The derivation of their integral begins with the mean streamwise momentum equation

$$\frac{\partial}{\partial x_3}\left(\nu\frac{\partial \bar{u}_1}{\partial x_3} - \overline{u_1' u_3'}\right) = I_0 + \frac{1}{\rho}\frac{\partial \bar{p}}{\partial x_1} + \frac{\partial \bar{u}_1}{\partial t}, \tag{1.2}$$

where x_1 and x_3 are the streamwise and wall-normal coordinates, u_1 and u_3 are the instantaneous velocities in the x_1 and x_3 directions, p is pressure, $\bar{\cdot}$ denotes time average, $\overline{u_1' u_3'}$ is the Reynolds shear stress, ν is viscosity, ρ is density, and I_0 is a term that contains the streamwise convection term and the streamwise diffusion term:

$$I_0 = \frac{\partial \overline{u_1 u_1}}{\partial x_1} + \frac{\partial \bar{u}_1 \bar{u}_3}{\partial x_3} - \nu\frac{\partial^2 \bar{u}_1}{\partial x_1^2}. \tag{1.3}$$

Integrating the above mean momentum equation, one gets the following decomposition of the skin friction coefficient (henceforth referred to as FIK):

$$C_f = \frac{4(1-\delta_1)}{Re_\delta} + 4\int_0^1 \left(1-\frac{x_3}{\delta}\right)\frac{-\overline{u_1'u_3'}}{U_\infty^2}\,\mathrm{d}\frac{x_3}{\delta} - \frac{2\delta}{U_\infty^2}\int_0^1 \left(1-\frac{x_3}{\delta}\right)^2\left(I_0+\frac{1}{\rho}\frac{\partial \bar{p}}{\partial x_1}+\frac{\partial \bar{u}_1}{\partial t}\right)\mathrm{d}\frac{x_3}{\delta}. \tag{1.4}$$

In this equation, $C_f = \tau_w/(0.5\rho U_\infty^2)$ and $Re_\delta = U_\infty\delta/\nu$, U_∞ is the freestream velocity, and δ is the boundary layer thickness. We examine the terms on the right-hand side of (1.4). The first two terms are the results of viscous diffusion and turbulent transport. These two terms do not appear in Kármán's integral and are internal to the boundary layer. They redistribute but do not inject or remove momentum from the boundary layer. The last term contains pressure gradient, flow acceleration/deceleration, and terms that are the result of the flow's evolution in the stream direction. It contains external fluxes, which contribute to the overall force balance. Following the discussion above, it was argued that the integral method would be more elegant if it contained only internal, Galilean-invariant terms. The above viewpoint was enunciated in Gao & Wu (2019) and Aghaei-Jouybari *et al.* (2022). The discussions in Fukagata *et al.* (2002) and Elnahhas & Johnson (2022) are also in line with the logic above, although the argument was less explicit.

To further illustrate this point, we apply the FIK integral to a laminar channel flow. Since the flow is laminar, $\overline{u_1'u_3'} = 0$, $I_0 = 0$ and $\partial\bar{u}_1/\partial t = 0$. It follows that (1.4) reduces to

$$C_f = \frac{4}{Re_b} - \frac{2}{3}\frac{\delta}{U_b^2}\frac{1}{\rho}\frac{\partial \bar{p}}{\partial x_1}, \tag{1.5}$$

where $C_f = \tau_w/(0.5\rho U_b^2)$ and $Re_b = U_b\delta/\nu$, U_b is the bulk velocity, and δ is the half-channel height. The laminar channel friction coefficient is known and is $C_f = 6/Re_b$. Equation (1.5) contains an internal term, i.e. the first term, and an external term, i.e. the second term. The equation suggests that 2/3 of the skin friction in a laminar channel is due to viscosity, and 1/3 is due to the imposed pressure gradient, which is not physical. To resolve this issue, one can invoke the following force balance (see (5)–(8) in Fukagata *et al.* 2002):

$$-\tau_w/\rho = \int_0^\delta \left(I_0+\frac{1}{\rho}\frac{\partial \bar{p}}{\partial x_1}+\frac{\partial \bar{u}_1}{\partial t}\right)\mathrm{d}x_3. \tag{1.6}$$

By performing the operation

$$\int_0^\delta\int_0^{x_3}\int_0^{x_3}\left(\text{Eq.}(1.2)-\alpha\,\frac{1}{\delta}\,\text{Eq.}(1.6)\right)\mathrm{d}x_3\,\mathrm{d}x_3\,\mathrm{d}x_3, \tag{1.7}$$

and taking $\alpha = 1$, one arrives at

$$C_f = \frac{6}{Re_b} \tag{1.8}$$

for laminar channel flow. Equation (1.8) contains one internal term only. It suggests that the skin friction in a laminar channel is due to the viscosity, which is the right-hand side.

Equation (1.7) also alludes to a longstanding issue of the integral methods. Because both (1.2) and (1.6) are exact, α in (1.7) is a free parameter, leading to ambiguity in

the derivation. For example, Fukagata *et al.* (2002) took $\alpha = 1$ to eliminate the pressure gradient force for channel, but took $\alpha = 0$ and kept the pressure gradient and other external momentum fluxes for boundary layers. We will elaborate on this issue in § 3.

Above, we delved into the consideration involving distinguishing between effects that are internal and external to the flow. Another consideration involves having a clear physical interpretation. Take again Kármán's integral equation as an illustrative example. Kármán's integral has a very clear interpretation. It describes the momentum balance.

We now turn our attention back to the integral methods. The integrals in Fukagata *et al.* (2002) and other follow-up works come from the Navier–Stokes equation. Consequently, the physical interpretations of terms within the Navier–Stokes equation seamlessly transfer to the integrals and their ensuing decompositions. This linkage is convenient, yet it does not fully encapsulate the entire narrative. Discussion on the physical interpretations of the integrals continues. Renard & Deck (2016) raised concerns about the interpretability of the triple integration in Fukagata *et al.* (2002), and they derived integrals grounded in kinetic energy. Yoon *et al.* (2016) developed integrals grounded in vorticity, linking the skin friction to the vortices in the flow. Elnahhas & Johnson (2022) interpreted the FIK integral as the second-order moment of momentum, and they derived integrals based on the first-order moment of momentum, which they interpret as the angular momentum. Ricco & Skote (2022) pointed out that the terms in the FIK integral depend sensitively on the integration limit, which brought uncertainty in the interpretation of the terms in the FIK integral. In addition to the integration limit, the adjustable parameters in the integrals are also a source of ambiguity: the prefactor one puts in front of the overall force balance when deriving the FIK integral, i.e. α in (1.7), the length scale in the angular momentum integral in Elnahhas & Johnson (2022), and the frame of reference in the kinetic energy integral in Renard & Deck (2016) are all adjustable parameters.

The preceding discussion outlines the two considerations driving the reformulation of existing integrals for smooth walls. Next, we explain the need for integrals for rough walls.

The friction on rough walls is different from that on smooth walls, τ_S. In addition to the skin friction on the bottom wall, roughness gives rise to roughness element drag force τ_R. In most high-Reynolds-number applications, τ_R is much larger than τ_S, therefore having a decomposition of τ_R in addition to a decomposition of τ_S is instructive. However, separate decompositions for τ_S and τ_R do not exist. Nikora *et al.* (2019) derived decompositions for rough walls. However, the integral involves $2\tau_S - \tau_R - 3\int_0^\delta \rho f_D(1 - x_3/\delta)^2\,\mathrm{d}x_3$, which is hard to interpret (see further details in § 3.2). This motivates us to seek new decompositions for rough walls. We require that the new decompositions satisfy the following requirements. First, they should be based on the Navier–Stokes equations, like the existing decompositions. Second, there should be separate decompositions for τ_S and τ_R. Third, the viscous term should be the only term when the decompositions are evaluated for laminar flow scenarios. Fourth, the decompositions should contain only terms that represent effects internal to the flow.

The subsequent sections of the paper are organized as follows. The double-averaged Navier–Stokes equations and the reformulation of the prior integral methods based on the double-averaged Navier–Stokes equations are summarized in §§ 2 and 3. New formulations for rough-wall friction are presented in § 4. The obtained bottom-wall skin friction coefficient decompositions and roughness drag coefficient decompositions are applied to flow over cubes with aligned and staggered arrangements. The details of the direct numerical simulations (DNS) data are presented in § 5, with the results shown in § 6. Further extensions of the integral methods are presented in § 7. Finally, we provide concluding remarks in § 8.

2. Double-averaged momentum equation and the force balance

We summarize the double-averaged momentum equation and the overall force balance. Here, double average refers to averages in time and the wall-parallel directions.

2.1. *Momentum equation*

The double-averaged streamwise momentum equation for rough-wall flows (Raupach & Shaw 1982; Nikora *et al.* 2013, 2019) reads

$$\frac{\partial\langle\bar{u}_1\rangle}{\partial t}+\frac{1}{\phi}\frac{\partial\phi\langle\bar{u}_1\rangle\langle\bar{u}_j\rangle}{\partial x_j}+\frac{1}{\phi}\frac{\partial\phi\langle\widetilde{\bar{u}}_1\widetilde{\bar{u}}_j\rangle}{\partial x_j}+\frac{1}{\phi}\frac{\partial\phi\langle\overline{u_1'u_j'}\rangle}{\partial x_j}$$
$$=-\frac{1}{\rho}\frac{1}{\phi}\frac{\partial\phi\langle\bar{p}\rangle}{\partial x_1}+\frac{1}{\rho}\frac{1}{A_f}\oint_S\bar{p}n_1\,\mathrm{d}S+\frac{1}{\phi}\frac{\partial}{\partial x_j}\left(\phi\left\langle\nu\frac{\partial\bar{u}_1}{\partial x_j}\right\rangle\right)-\frac{1}{A_f}\oint_S\nu\frac{\partial\bar{u}_1}{\partial x_j}n_j\,\mathrm{d}S+f_x, \tag{2.1}$$

where x_1, x_2, x_3 are the streamwise, spanwise and wall-normal directions, u_1, u_2 and u_3 are the instantaneous fluid velocities in the x_1, x_2, x_3 directions, p is the pressure, ρ is the density, f_x is a body force that contains the mean pressure gradient, $\phi=A_f/A_0$ is the roughness porosity (with A_f the fluid occupied planar area that is a function of x_3), A_0 is the total planar area, S marks the boundary of the fluid area, and n_j is the unit vector normal to the solid boundary directed into the fluid. Here, $\bar{\cdot}$ denotes time average, $\langle\cdot\rangle$ denotes the intrinsic spatial average, defined as

$$\langle\theta\rangle=\frac{1}{A_f}\iint_{A_f}\theta\,\mathrm{d}x_1\,\mathrm{d}x_2, \tag{2.2}$$

$\theta'=\theta-\bar{\theta}$ is fluctuation about the time average, and $\widetilde{\bar{\theta}}=\bar{\theta}-\langle\bar{\theta}\rangle$ is the deviation of the time average from the double average. Figure 1 is a sketch illustrating these concepts.

We may rewrite the double-averaged x_1 momentum equation as

$$\frac{\partial}{\partial x_3}\left(\phi\left\langle\nu\frac{\partial\bar{u}_1}{\partial x_3}\right\rangle\right)-\frac{\partial\phi\langle\overline{u_1'u_3'}\rangle}{\partial x_3}-\frac{\partial\phi\langle\widetilde{\bar{u}}_1\widetilde{\bar{u}}_3\rangle}{\partial x_3}-I_x+f_D+\phi f_x=0, \tag{2.3}$$

where the term $\langle\overline{u_1'u_3'}\rangle$ is the Reynolds shear stress, $\langle\widetilde{\bar{u}}_1\widetilde{\bar{u}}_3\rangle$ is the dispersive stress, I_x contains the horizontal convection and dispersion,

$$I_x=\phi\frac{\partial\langle\bar{u}_1\rangle}{\partial t}+\frac{\partial\phi\langle\bar{u}_1\rangle\langle\bar{u}_j\rangle}{\partial x_j}+\frac{\partial\phi\langle\widetilde{\bar{u}}_1\widetilde{\bar{u}}_1\rangle}{\partial x_1}+\frac{\partial\phi\langle\widetilde{\bar{u}}_1\widetilde{\bar{u}}_2\rangle}{\partial x_2}+\frac{\partial\phi\langle\overline{u_1'u_1'}\rangle}{\partial x_1}$$
$$+\frac{\partial\phi\langle\overline{u_1'u_2'}\rangle}{\partial x_2}-\frac{\partial}{\partial x_1}\left(\phi\left\langle\nu\frac{\partial\bar{u}_1}{\partial x_1}\right\rangle\right)-\frac{\partial}{\partial x_2}\left(\phi\left\langle\nu\frac{\partial\bar{u}_1}{\partial x_2}\right\rangle\right)+\frac{1}{\rho}\frac{\partial\phi\langle\bar{p}\rangle}{\partial x_1}, \tag{2.4}$$

and f_D contains the form drag and viscous drag on the roughness elements per unit volume,

$$f_D=\underbrace{\phi\frac{1}{A_f}\frac{1}{\rho}\oint_S\bar{p}n_1\,\mathrm{d}S}_{\textit{form drag}}\underbrace{-\phi\frac{1}{A_f}\oint_S\nu\frac{\partial\bar{u}_1}{\partial x_j}n_j\,\mathrm{d}S}_{\textit{viscous drag}}. \tag{2.5}$$

Consider the rough walls with discrete roughness elements. The friction consists of two parts: the roughness element drag and the skin friction on the bottom wall. The roughness

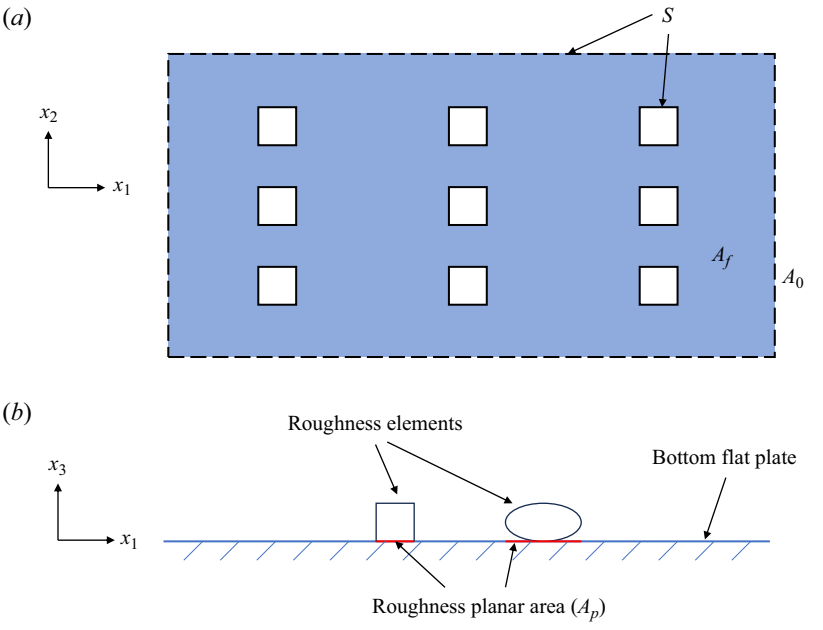

Figure 1. (*a*) An illustration of the multi-connected area for the spatial integration in the roughness layer. The planar area A_0 is bounded by the dashed line. The fluid area A_f is blue and surrounds the white, roughness-occupied area. Their ratio A_f/A_0 gives the roughness porosity ϕ. The fluid boundary S consists of the outer boundary (dashed) and the inner boundary (solid). (*b*) An illustration of the roughness planar area A_p, i.e. the red area under the roughness elements. The ratio A_p/A_0 gives the planar coverage density λ_p.

element drag and the corresponding drag coefficient are defined as

$$\tau_R = -\int_0^h \rho f_D \,\mathrm{d}x_3, \quad C_R = \frac{1}{\lambda_p}\frac{\tau_R}{0.5\rho U_r^2}, \tag{2.6a,b}$$

where h is the roughness height, U_r is some reference velocity, $\lambda_p = A_p/A_0$ is the planar roughness packing density and is not a function of x_3, and A_p is the roughness planar area as shown in figure 1(*b*) and equals $1-\phi$ in for cubic roughness. The bottom-wall skin friction and the corresponding drag coefficient are defined as

$$\tau_S = \left[\rho\phi\left\langle \nu\frac{\partial \bar{u}_1}{\partial x_3}\right\rangle\right]_{x_3=0}, \quad C_S = \frac{\tau_S}{0.5\rho U_r^2}. \tag{2.7a,b}$$

The common choices of the reference velocity U_r are the freestream velocity U_∞, the centreline velocity U_0, and the bulk velocity $U_b = \int_0^1 \phi\langle\bar{u}_1\rangle \,\mathrm{d}(x_3/\delta)$. Note that the freestream velocity of boundary layers is an external variable that stays the same independently of conditions of a boundary layer. In contrast, the centreline and bulk velocities in internal flows are not independent of the conditions on the wall and thus are internal variables. The overall drag is given by $\tau_R + \tau_S$, and the overall friction coefficient C_f is

$$C_f = \frac{\tau_S + \tau_R}{0.5\rho U_r^2} = C_S + \lambda_p C_R, \tag{2.8}$$

such that $C_f = C_S + \lambda_p C_R$ can be used to evaluate C_f when C_S and C_R are available.

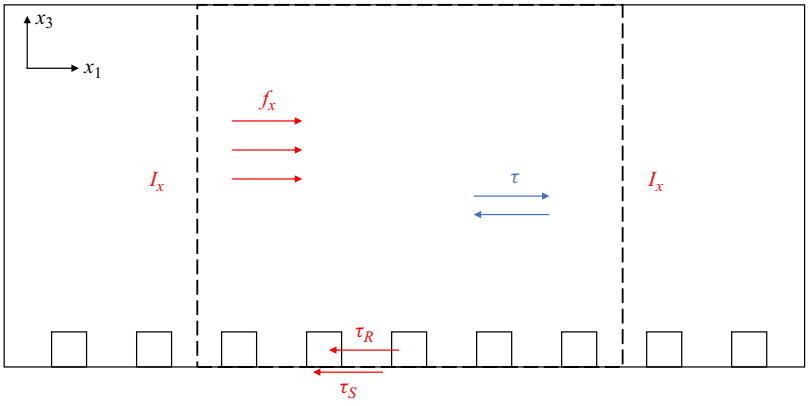

Figure 2. Schematic of flow over a rough surface: f_x, I_x, τ_S, τ_R are the external forces; $\tau = \phi\langle\nu\,\partial\bar{u}_1/\partial x_3\rangle - \phi\langle\overline{u_1'u_3'}\rangle - \phi\langle\widetilde{\bar{u}}_1\widetilde{\bar{u}}_3\rangle$ is the internal fluid stress.

2.2. *Force balance*

The overall force balance can be obtained by integrating the double-averaged momentum equation (2.3) from $x_3 = 0$ to $x_3 = \delta$:

$$\int_0^\delta \left[\frac{\partial}{\partial x_3}\left(\phi\left\langle\nu\frac{\partial\bar{u}_1}{\partial x_3}\right\rangle\right) - \frac{\partial\phi\langle\overline{u_1'u_3'}\rangle}{\partial x_3} - \frac{\partial\phi\langle\widetilde{\bar{u}}_1\widetilde{\bar{u}}_3\rangle}{\partial x_3} - I_x + f_D + \phi f_x\right]\mathrm{d}x_3 = 0. \tag{2.9}$$

The first term gives the viscous friction on the flat bottom wall:

$$\int_0^\delta \frac{\partial}{\partial x_3}\left(\phi\left\langle\nu\frac{\partial\bar{u}_1}{\partial x_3}\right\rangle\right)\mathrm{d}x_3 = \phi\left\langle\nu\frac{\partial\bar{u}_1}{\partial x_3}\right\rangle\Big|_0^\delta = -\tau_S/\rho, \tag{2.10}$$

where we have neglected the velocity gradient at $x_3 = \delta$. The second and third terms, i.e. the Reynolds and dispersive stress terms, are internal terms and do not contribute to the overall force balance. The integration of f_D gives the roughness drag $-\tau_R/\rho$ per (2.6*a*,*b*). Hence the overall force balance is

$$-\tau_S/\rho - \tau_R/\rho + \int_0^\delta \phi f_x\,\mathrm{d}x_3 - \int_0^\delta I_x\,\mathrm{d}x_3 = 0. \tag{2.11}$$

Figure 2 provides a visual illustration of the force balance. The momentum flux on the left, right and top boundaries, denoted as I_x in the figure, and the forcing, denoted by f_x in the figure, are balanced by the wall shear stress and the roughness drag force, denoted by τ_S and τ_R in the figure. The viscous force, Reynolds stress and dispersive stress are internal forces; they redistribute the momentum within the flow, but do not contribute to the overall force balance at the scale of the whole flow.

3. Prior integrals based on the double-averaged Navier–Stokes equation

In this section, we re-derive the prior integrals, including the mean momentum integral (Fukagata *et al.* 2002; Nikora *et al.* 2019), the angular momentum integral (Elnahhas & Johnson 2022), and the kinetic energy integral (Renard & Deck 2016), based on the double-averaged Navier–Stokes equation. It will be clear that the prior integrals do not

separate τ_S and τ_R. We will also review previous applications of these integrals and their weaknesses to further motivate the present work on rough walls. For brevity, we will utilize the first letters of the three leading authors' names when referring to the NSC method as outlined in Nikora *et al.* (2019).

3.1. *Momentum-based integral*

The momentum-based integrals are pioneered by Fukagata *et al.* (2002). Integrating the double-averaged momentum equation (2.3), we arrive at the following decomposition of the wall shear stress:

$$\tau_S/\rho = \frac{2U_b^2}{Re_b} + 2\int_0^1 \left(1-\frac{x_3}{\delta}\right)\left(-\phi\langle\overline{u_1'u_3'}\rangle - \phi\langle\widetilde{\widetilde{u}}_1\widetilde{\widetilde{u}}_3\rangle\right)\mathrm{d}\frac{x_3}{\delta} + \int_0^1 \left(1-\frac{x_3}{\delta}\right)^2(\phi f_x + f_D - I_x)\delta\,\mathrm{d}\frac{x_3}{\delta}. \tag{3.1}$$

This FIK decomposition proves to be a valuable diagnostic tool, and many have applied it for flow analysis. Deck *et al.* (2014) examined the integrals for flat-plate boundaries for a wide range of Reynolds numbers ($3060 \le Re_\theta \le 13\,650$). They found that about 80 % of the skin friction in high-Reynolds-number boundary layers is due to turbulent motions. Moreover, the large-scale motions with streamwise wavelengths $\lambda_x > \delta$ and $\lambda_x > 2\delta$ account for approximately 60 % and 45 % of the skin friction, respectively. de Giovanetti, Hwang & Choi (2016) studied the skin friction generated by self-similar energy-containing motions up to a friction Reynolds number of approximately 4000. Their findings indicated that the removal of very-large-scale and large-scale motions resulted in only a minimal 5 %–8 % reduction in skin friction. The utility of the FIK method is not limited to canonical boundary layer flows; it also serves as a reliable tool for assessing the effectiveness of drag-reduction techniques. For example, an analysis by Iwamoto *et al.* (2005) suggested that eliminating near-wall turbulence within $x_3^+ < 10$ could lead to a substantial 35 % drag reduction at $Re_\tau = 10^5$. The FIK integral method has also been used for rough-wall boundary layers (Bannier, Garnier & Sagaut 2015; Nikora *et al.* 2019; Zhang *et al.* 2021) and compressible flows (Gomez, Flutet & Sagaut 2009), where additional terms emerge due to the complexity of these flow regimes. In § 3.2, we will delve further into the integral method proposed by Nikora *et al.* (2019) for rough walls.

The FIK integral has received criticism, and alternative integrals have been explored. In the following, we review these criticisms and the alternatives integrals. The first criticism concerns the triple integration. Renard & Deck (2016) found the triple integration hard to interpret. They argued that the product of a force and a length in the second integration has the dimension of energy, and developed integrals grounded in kinetic energy. Elnahhas & Johnson (2022) pointed out that the triple integration gives the second moment of momentum. They argued that instead of the second moment, the first moment of momentum is more straightforward to interpret. The second criticism concerns the integration limit in the case of boundary layer flow. Ricco & Skote (2022) showed that the value of the terms in the FIK integral depends on the upper integration limit, which is a source of uncertainty. In addition to the usual δ_{99}, Wenzel, Gibis & Kloker (2022) compared different choices of the upper integration limit, and found that their results do not depend qualitatively on the choice of the integration limit. Xu, Wang & Chen (2022) also noticed that the exact value of the upper integration limit is not critical for drawing general conclusions, at least in their study of hypersonic boundary layers.

Nonetheless, to circumvent the issue of the integration limit, Renard & Deck (2016) turned to the moving reference frame, and Elnahhas & Johnson (2022) resorted to the deficit equation. In both scenarios, the contributions of the far field to the terms in the integrals approach 0 as the upper integration limits are approaching infinity. The third criticism concerns the weighting, i.e. $(1 - x_3/\delta)$ and $(1 - x_3/\delta)^2$ in the integral (Fukagata *et al.* 2024). This weighting is a result of the triple integration. It emphasizes the wall layer, and de-emphasizes the logarithmic and outer layers. Whether such weighting is physical is debated. The existing literature shows that as the Reynolds number increases, the turbulent motions in the logarithmic and outer layers become increasingly more important (Smits, McKeon & Marusic 2011; Marusic & Monty 2019). These large-scale and vary-large-scale motions influence the inner dynamics not only through superposition, but also through amplitude modulation (Marusic, Mathis & Hutchins 2010; Yang & Howland 2018). Besides, the weighting in the FIK integral poses challenges to laboratory data, which usually incur large uncertainties near the wall (Mehdi *et al.* 2014; Volino & Schultz 2018; Xia, Zhang & Yang 2021). To overcome this issue, Volino & Schultz (2018) and Xia *et al.* (2021) proposed methods that allow one to determine the wall shear stress without access to the data in the near-wall region. The last criticism concerns the use of the overall force balance in the derivation, which was already highlighted in § 1.

3.2. *The NSC method*

The NSC method was introduced in Nikora *et al.* (2019). The method extends the FIK integral to rough-wall boundary layers. The integral reads

$$\frac{8\tau_R}{\rho U_b^2} = \frac{1}{N}\frac{48}{Re_b} + \frac{1}{N}\frac{48}{\delta^2 U_b^2}\int_0^\delta (\delta - x_3)(-\phi\langle\overline{u_1' u_3'}\rangle - \phi\langle\widetilde{\bar{u}}_1\widetilde{\bar{u}}_3\rangle)\,\mathrm{d}x_3 + \frac{1}{N}\frac{24}{\delta^2 U_b^2}\int_0^\delta (\delta - x_3)^2\left(\phi f_x - I_x - \frac{1}{\delta}\int_0^\delta (\phi f_x - I_x)\,\mathrm{d}x_3\right)\mathrm{d}x_3, \tag{3.2}$$

where

$$N = \left(2\tau_S - \tau_R - 3\int_0^\delta \rho f_D (1 - x_3/\delta)^2\,\mathrm{d}x_3\right)/\tau_R \tag{3.3}$$

is interpreted as the flow–rough-wall interaction (Nikora *et al.* 2019). Nikora *et al.* (2019) applied the decomposition in (3.2) and analysed the river-bed friction. They found that both the roughness-induced and large-scale secondary-currents-induced dispersive stress may play significant roles in generating bed friction at sufficiently high Reynolds numbers.

Equation (3.2) has the same weaknesses as FIK. Additionally, the decomposition in (3.2) does not distinguish between the skin friction on the bottom wall and the drag force on the roughness elements.

3.3. *Angular momentum integral*

The angular momentum integral (AMI) is introduced in Elnahhas & Johnson (2022). To derive the AMI, we subtract the freestream momentum equation

$$\frac{\partial U_\infty}{\partial t} + U_\infty\frac{\partial U_\infty}{\partial x_1} = -\frac{1}{\rho}\frac{\partial P_\infty}{\partial x_1} \tag{3.4}$$

from the double-averaged streamwise momentum equation (2.3). This gives

$$\frac{\partial}{\partial x_3}\left(\phi\left\langle\nu\frac{\partial\bar{u}_1}{\partial x_3}\right\rangle\right)-\frac{\partial\phi\langle\overline{u_1'u_3'}\rangle}{\partial x_3}-\frac{\partial\phi\langle\widetilde{\bar{u}}_1\widetilde{\bar{u}}_3\rangle}{\partial x_3}$$
$$+\left(\frac{\partial(U_\infty-\langle\bar{u}_1\rangle)\phi\langle\bar{u}_j\rangle}{\partial x_j}+(U_\infty-\phi\langle\bar{u}_1\rangle)\frac{\partial U_\infty}{\partial x_1}\right)-I_{x,d}+f_D+\phi f_x=0, \tag{3.5}$$

where $I_{x,d}$ contains both the streamwise inhomogeneity terms and the freestream terms:

$$I_{x,d}=-\left(\frac{\partial(U_\infty-\phi\langle\bar{u}_1\rangle)}{\partial t}+\frac{1}{\rho}\frac{\partial(P_\infty-\phi\langle\bar{p}\rangle)}{\partial x_1}\right)$$
$$+\frac{\partial\phi\langle\widetilde{\bar{u}}_1\widetilde{\bar{u}}_1\rangle}{\partial x_1}+\frac{\partial\phi\langle\widetilde{\bar{u}}_1\widetilde{\bar{u}}_2\rangle}{\partial x_2}+\frac{\partial\phi\langle\overline{u_1'u_1'}\rangle}{\partial x_1}+\frac{\partial\phi\langle\overline{u_1'u_2'}\rangle}{\partial x_2}$$
$$-\frac{\partial}{\partial x_1}\left(\phi\left\langle\nu\frac{\partial\bar{u}_1}{\partial x_1}\right\rangle\right)-\frac{\partial}{\partial x_2}\left(\phi\left\langle\nu\frac{\partial\bar{u}_1}{\partial x_2}\right\rangle\right). \tag{3.6}$$

Integrating the deficit momentum equation (3.5) premultiplied by (x_3-l) directly gives the AMI:

$$\frac{\tau_S}{\rho U_\infty^2}=\frac{1}{Re_l}+\int_0^\infty\frac{(-\phi\langle\overline{u_1'u_3'}\rangle-\phi\langle\widetilde{\bar{u}}_1\widetilde{\bar{u}}_3\rangle)}{U_\infty^2 l}\,\mathrm{d}x_3$$
$$+\left(\frac{\partial\theta_l}{\partial x_1}+\frac{\theta_l-\theta}{l}\frac{\partial l}{\partial x_1}+\frac{2\theta_l}{U_\infty}\frac{\partial U_\infty}{\partial x_1}\right)+\frac{\partial\theta_{l2}}{\partial x_2}+\frac{\theta_3}{l}+\frac{\delta_l^*}{U_\infty}\frac{\partial U_\infty}{\partial x_1}$$
$$+\frac{1}{U_\infty^2}\int_0^\infty\left(1-\frac{x_3}{l}\right)(-I_{x,d}+f_D+\phi f_x)\,\mathrm{d}x_3. \tag{3.7}$$

Here, Re_l is the Reynolds number based on the freestream velocity U_∞ and the origin location l, θ and θ_3 are the momentum thicknesses,

$$\theta=\int_0^\infty\left(1-\frac{\langle\bar{u}_1\rangle}{U_\infty}\right)\frac{\phi\langle\bar{u}_1\rangle}{U_\infty}\,\mathrm{d}x_3,\quad \theta_3=\int_0^\infty\left(1-\frac{\langle\bar{u}_1\rangle}{U_\infty}\right)\frac{\phi\langle\bar{u}_3\rangle}{U_\infty}\,\mathrm{d}x_3, \tag{3.8a,b}$$

and δ_l^*, θ_l, θ_{l2} are the modified displacement and momentum thicknesses:

$$\delta_l^*=\int_0^\infty\left(1-\frac{x_3}{l}\right)\left(1-\frac{\phi\langle\bar{u}_1\rangle}{U_\infty}\right)\mathrm{d}x_3, \tag{3.9}$$

$$\theta_l=\int_0^\infty\left(1-\frac{x_3}{l}\right)\left(1-\frac{\langle\bar{u}_1\rangle}{U_\infty}\right)\frac{\phi\langle\bar{u}_1\rangle}{U_\infty}\,\mathrm{d}x_3,$$
$$\theta_{l2}=\int_0^\infty\left(1-\frac{x_3}{l}\right)\left(1-\frac{\langle\bar{u}_1\rangle}{U_\infty}\right)\frac{\phi\langle\bar{u}_2\rangle}{U_\infty}\,\mathrm{d}x_3. \tag{3.10a,b}$$

Equation (3.7) holds for arbitrary non-zero l. Elnahhas & Johnson (2022) propose to pick l such that

$$\frac{1}{Re_l}=\frac{0.332}{\sqrt{Re_x}}=\frac{0.221}{Re_\theta}=\frac{0.571}{Re_{\delta^*}}=\frac{1.63}{Re_\delta}, \tag{3.11}$$

which is the friction coefficient of a laminar flat-plate boundary layer. Here, Re_x, Re_θ, Re_{δ^*}, Re_δ are the Reynolds numbers based on the streamwise distance, the momentum thickness, the displacement thickness and the boundary layer thickness, respectively. This choice allows one to compare the laminar and turbulent boundary layers.

3.4. *Kinetic energy integral*

The triple integration in Fukagata *et al.* (2002) gives rise to weightings that de-emphasize the logarithmic layer, which, as Renard & Deck (2016) argued, is undesirable. Attempts have been made so that fewer integrations are needed. A noteworthy work along this direction is the kinetic energy integral in Renard & Deck (2016), which requires a single integration. The 'trick' is to integrate the premultiplied mean momentum equation in a reference frame moving with the freestream. The resulting integral can be interpreted as the mean kinetic energy. The integral has been applied to study the effects of compressibility (Li *et al.* 2019), mean pressure gradient (Fan *et al.* 2020), chemical reactions (Passiatore *et al.* 2021) and the transition (Marxen & Zaki 2019).

Again, we re-derive the integral based on the double-averaged Navier–Stokes equation. Following Renard & Deck (2016), we premultiply the double-averaged Navier–Stokes equation by $(\phi\langle\bar{u}_1\rangle - U_\infty)$, and integrate the equation. This leads to

$$U_\infty \tau_S/\rho = \int_0^\infty \nu \left(\frac{\partial \phi\langle\bar{u}_1\rangle}{\partial x_3}\right)^2 \mathrm{d}x_3 + \int_0^\infty (-\phi\langle\overline{u_1' u_3'}\rangle - \phi\langle\widetilde{\bar{u}}_1\widetilde{\bar{u}}_3\rangle)\frac{\partial \phi\langle\bar{u}_1\rangle}{\partial x_3}\,\mathrm{d}x_3 - \int_0^\infty (\phi\langle\bar{u}_1\rangle - U_\infty)(-I_x + f_D + \phi f_x)\,\mathrm{d}x_3. \tag{3.12}$$

The first term on the right-hand side is the modified viscous dissipation, the second term is the modified production of the turbulent and dispersive kinetic energy, and the third term is the additional energy loss due to $(-I_x + f_D + \phi f_x)$. For channel flows, the integration of (2.3) should be performed by premultiplying $(\phi\langle\bar{u}_1\rangle - U_b)$ (Renard & Deck 2016), which gives

$$U_b \tau_S/\rho = \int_0^\delta \nu \left(\frac{\partial \phi\langle\bar{u}_1\rangle}{\partial x_3}\right)^2 \mathrm{d}x_3 + \int_0^\delta (-\phi\langle\overline{u_1' u_3'}\rangle - \phi\langle\widetilde{\bar{u}}_1\widetilde{\bar{u}}_3\rangle)\frac{\partial \phi\langle\bar{u}_1\rangle}{\partial x_3}\,\mathrm{d}x_3 - \int_0^\delta (\phi\langle\bar{u}_1\rangle - U_b)(-I_x + f_D + \phi f_x)\,\mathrm{d}x_3. \tag{3.13}$$

The integral holds for any U_r that one puts in the premultiplier $(\phi\langle\bar{u}_1\rangle - U_r)$. Like the prefactor α in the FIK integral, and the length scale l in the AMI, U_r here is an adjustable parameter.

4. Present work

We see from § 3 that the existing integrals do not separate τ_S and τ_R. Furthermore, all of them contain adjustable parameters, which is a source of ambiguity. In this section, we aim to reformulate the prior integrals such that they overcome these two issues. Considering a decomposition that expresses τ_S and τ_R as a function of other terms in the overall force balance equation, we also require that the decompositions that we derive contain only terms that represent effects internal to the flow. Furthermore, we require that the viscous term, if present, is the only term surviving when the decompositions are evaluated for laminar flows.

4.1. *Kinetic-energy-based integral*

We multiply the mean momentum equation (2.3) with $(\phi\langle\bar{u}_1\rangle - U_w)$ and then integrate:

$$U_w\tau_S/\rho + \int_0^\delta (\phi\langle\bar{u}_1\rangle - U_w) f_D \,\mathrm{d}x_3 + \int_0^\delta (\phi\langle\bar{u}_1\rangle - U_w)\phi f_x \,\mathrm{d}x_3 - \int_0^\delta (\phi\langle\bar{u}_1\rangle - U_w) I_x \,\mathrm{d}x_3$$
$$= \int_0^\delta \left[\nu \left(\frac{\partial \phi\langle\bar{u}_1\rangle}{\partial x_3} \right)^2 - \phi\overline{\langle u_1' u_3'\rangle} \frac{\partial \phi\langle\bar{u}_1\rangle}{\partial x_3} - \phi\langle\widetilde{\bar{u}}_1\widetilde{\bar{u}}_3\rangle \frac{\partial \phi\langle\bar{u}_1\rangle}{\partial x_3} \right] \mathrm{d}x_3. \tag{4.1}$$

Here, the flow type (i.e. whether the flow is a boundary layer or a channel) is left unspecified. We will see soon that our decompositions do not depend on the flow type. In the integrals above, δ is the boundary layer height and should be sufficiently high such that the Reynolds shear stress and the dispersive stress are approximately 0 there. A convenient definition could be $\delta = 1.5\delta_{99}$ (Wenzel *et al.* 2022; Xu *et al.* 2022) to enable qualitative results. Considering that the far-field contribution to these two stresses is 0, the integration will not depend sensitively on the value of δ as long as it is sufficiently large. For now, U_w is left undetermined. Equation (4.1) can be interpreted as the kinetic energy equation in the reference frame that moves at speed U_w in the $+x_1$ direction. The terms on the left- and right-hand sides are the external energy source terms and internal energy loss terms, respectively. The external energy source terms are dependent on the choice of the reference frame. The internal energy loss terms are due to viscosity, turbulence and mean flow inhomogeneity, and therefore do not depend on the reference frame. The first two terms on the left-hand side are the terms due to the bottom viscous friction and the roughness drag force, and they contain the skin friction coefficient and the roughness drag coefficient information. The third and fourth terms are energy inputs due to the forcing term and the streamwise evolution of the flow. The terms on the left-hand side are positive or negative depending on U_w. When a term is positive, it represents a positive source; and when a term is negative, it represents a negative source. The terms on the right-hand side are almost always positive, representing energy loss due to mean flow dissipation, turbulent production, and the production of dispersive kinetic energy.

The next step is to remove terms that represent external effects and isolate the surface skin friction term and the roughness drag coefficient term. We do that via U_w. Specifically, the following U_w eliminates the terms representing external effects and isolates the skin friction term:

$$U_w \equiv U_{w,S} = \frac{\displaystyle\int_0^\delta \phi\langle\bar{u}_1\rangle (f_D + \phi f_x - I_x)\,\mathrm{d}x_3}{\displaystyle\int_0^\delta (f_D + \phi f_x - I_x)\,\mathrm{d}x_3}$$
$$= \frac{1}{\tau_S}\int_0^\delta \rho\phi\langle\bar{u}_1\rangle (f_D + \phi f_x - I_x)\,\mathrm{d}x_3, \tag{4.2}$$

where we have invoked the force balance in (2.11). The values of $U_{w,S}$ for some specific flow scenarios are listed in table 1. For a fully developed plane channel flow, $f_D = 0$, $I_x = 0$, and (4.2) gives $U_{w,S} = U_b$. For a zero pressure gradient flat-plate boundary layer, $f_D = 0$, $f_x = 0$, and (4.2) gives $U_{w,S} = \int_0^\delta (\rho\phi\langle\bar{u}_1\rangle(-I_x)/\tau_S)\,\mathrm{d}x_3$. For a fully developed channel flow in the fully rough regime with $h \ll \delta$, $I_x = 0$, the integration of $\phi\langle\bar{u}_1\rangle f_D$ is small, and (4.2) gives $U_{w,S} \approx (\tau_R/\tau_S + 1)U_b$. Equations (4.1) and (4.2) together give the

Flow scenarios		$U_{w,S}$	$U_{w,R}$
Plane channel	$\begin{cases} f_D = 0, \\ I_x = 0 \end{cases}$	U_b	N/A
Flat-plate ZPGBL	$\begin{cases} f_D = 0, \\ f_x = 0 \end{cases}$	$\displaystyle\int_0^\delta \frac{\rho\phi\langle\bar{u}_1\rangle(-I_x)}{\tau_S}\,\mathrm{d}x_3$	N/A
Transitionally rough channel	$\begin{cases} h \ll \delta, \\ I_x = 0 \end{cases}$	$(1+\tau_R/\tau_S)U_b$	$(\tau_S/\tau_R+1)U_b$
Fully rough channel	$\begin{cases} \tau_S \ll \tau_R, \\ h \ll \delta, \\ I_x = 0 \end{cases}$	∞	U_b
Fully rough ZPGBL	$\begin{cases} \tau_S \ll \tau_R, \\ h \ll \delta, \\ f_x = 0 \end{cases}$	∞	$\displaystyle\int_0^\delta \frac{\rho\phi\langle\bar{u}_1\rangle(-I_x)}{\tau_R}\,\mathrm{d}x_3$

Table 1. Values of $U_{w,S}$ and $U_{w,R}$ for some special flow scenarios. We assume that the flows are fully developed. ZPGBL is short for zero pressure gradient boundary layer.

following decomposition of the bottom viscous friction coefficient C_S:

$$(0.5U_{w,S}U_r^2)C_S = \int_0^\delta \left[\nu\left(\frac{\partial\phi\langle\bar{u}_1\rangle}{\partial x_3}\right)^2 - \phi\langle\overline{u_1'u_3'}\rangle\frac{\partial\phi\langle\bar{u}_1\rangle}{\partial x_3} - \phi\langle\widetilde{\bar{u}}_1\widetilde{\bar{u}}_3\rangle\frac{\partial\phi\langle\bar{u}_1\rangle}{\partial x_3}\right]\mathrm{d}x_3, \tag{4.3}$$

where U_r is some reference velocity.

Similarly, we can isolate the roughness drag and eliminate the terms that represent external effects by choosing the following U_w:

$$U_w \equiv U_{w,R} = \frac{1}{\tau_R}\int_0^\delta \rho\phi\langle\bar{u}_1\rangle(f_D + \phi f_x - I_x)\,\mathrm{d}x_3. \tag{4.4}$$

Again, we have also invoked the force balance in (2.11). This velocity obviously exists only for a rough-wall flow, for which $\tau_R \neq 0$. Its values for a few specific flow scenarios are listed in table 1. For a fully-developed channel flow in the transitionally rough regime with $h \ll \delta$, the integration of $\rho\phi\langle\bar{u}_1\rangle f_D$ is small, $I_x = 0$, and we have $U_{w,R} \approx (1+\tau_S/\tau_R)U_b$. For fully developed channels in the fully rough regime with $h \ll \delta$, $I_x = 0$, the integration of $\rho\phi\langle\bar{u}_1\rangle f_D$ is small, $\tau_R \gg \tau_S$, and we have $U_{w,R} \approx U_b$. Invoking (4.1) and (4.4), we have the following decomposition of the roughness element drag coefficient:

$$(0.5U_{w,R}U_r^2)\lambda_p C_R = \int_0^\delta \left[\nu\left(\frac{\partial\phi\langle\bar{u}_1\rangle}{\partial x_3}\right)^2 - \phi\langle\overline{u_1'u_3'}\rangle\frac{\partial\phi\langle\bar{u}_1\rangle}{\partial x_3} - \phi\langle\widetilde{\bar{u}}_1\widetilde{\bar{u}}_3\rangle\frac{\partial\phi\langle\bar{u}_1\rangle}{\partial x_3}\right]\mathrm{d}x_3. \tag{4.5}$$

We now assess whether the decompositions presented in (4.3) and (4.5) meet our requirements. First and foremost, (4.3) and (4.5) stand as distinct decompositions for the skin friction coefficient C_S and the roughness drag coefficient C_R, respectively. Second, ambiguities in the derivation process are removed, and we have unique choices for U_w. Third, we have eliminated terms dependent on the reference frame, retaining only those

effects that are internal to the flow. Finally, the first term in both equations is the sole surviving term when the two decompositions are evaluated for laminar flows above a flat plate, regardless of whether the flow occurs in a channel or a boundary layer.

Before we proceed to the next subsection, we comment on the choice of keeping the terms that represent internal effects and eliminating the terms that represent external effects in the decompositions in (4.3) and (4.5). First and foremost, we should note that the external effects are only formally eliminated, as they are still contained in our specific choices of U_w (or l and α in the following sections). We can also explicitly keep the terms that represent external effects and eliminate the terms that represent internal effects. To do that, we divide both sides of (4.1) by U_w, and take U_w to infinity. The resulting expression, however, reduces to the overall force balance, or Kármán's equation, which is not very instructive.

4.2. *Angular-momentum-based integral*

We premultiply the mean momentum equation with $(x_3 - l)$ and integrate:

$$l\tau_S/\rho + \int_0^\delta (x_3 - l) f_D \,\mathrm{d}x_3 + \int_0^\delta (x_3 - l)\phi f_x \,\mathrm{d}x_3 + \int_0^\delta (x_3 - l)(-I_x)\,\mathrm{d}x_3 = \int_0^\delta \left(\nu \frac{\partial \phi \langle \bar{u}_1 \rangle}{\partial x_3} - \phi \langle \overline{u_1' u_3'} \rangle - \phi \langle \widetilde{\bar{u}}_1 \widetilde{\bar{u}}_3 \rangle \right) \mathrm{d}x_3. \tag{4.6}$$

Here, l is the location of the rotation axis. The terms on the left-hand side encompass the external sources of angular momentum, which include contributions from the surface skin friction, the roughness drag force, the evolution of the flow in the streamwise direction, and external forcing. These terms depend on the location of the axis l. In contrast, the terms on the right-hand side represent internal losses of angular momentum due to mean flow gradient, Reynolds shear stress and dispersive stress, and they do not depend on the axis location.

As before, the next step is to eliminate the terms representing external effects and isolate the skin friction and drag force terms via the free parameter in the integral l. The following l isolates τ_S:

$$l \equiv l_S = \frac{1}{\tau_S} \int_0^\delta \rho x_3 (f_D + \phi f_x - I_x)\,\mathrm{d}x_3. \tag{4.7}$$

The values of l_S for a few specific flow scenarios are listed in table 2. Equations (4.6) and (4.7) together give the angular-momentum-based decomposition of the skin friction coefficient

$$C_S = \frac{2}{Re_{l,S}} \frac{U_\delta}{U_r} + \frac{2}{U_r^2 l_S} \int_0^\delta (-\phi \langle \overline{u_1' u_3'} \rangle - \phi \langle \widetilde{\bar{u}}_1 \widetilde{\bar{u}}_3 \rangle)\,\mathrm{d}x_3, \tag{4.8}$$

where U_δ is the velocity at $x_3 = \delta$, and $Re_{l,S} = l_S U_r/\nu$. The first term on the right-hand side of (4.8) represents the laminar contribution and is the only term surviving when the equation is evaluated for laminar-flow and flat-plate scenarios.

Similarly, we can isolate the roughness drag coefficient and eliminate the terms representing external effects by taking the following l:

$$l \equiv l_R = \frac{1}{\tau_R/\rho} \left(\int_0^\delta x_3 (f_D + \phi f_x - I_x)\,\mathrm{d}x_3 \right). \tag{4.9}$$

Flow scenario		l_S	l_R
Plane channel	$\begin{cases} f_D = 0, \\ I_x = 0 \end{cases}$	$\delta/2$	N/A
Flat-plate ZPGBL	$\begin{cases} f_D = 0, \\ f_x = 0 \end{cases}$	$\displaystyle\int_0^\delta \rho x_3(-I_x)/\tau_S \,\mathrm{d}x_3$	N/A
Transitionally rough channel	$\begin{cases} h \ll \delta, \\ I_x = 0 \end{cases}$	$(1+\tau_R/\tau_S)\delta/2$	$(\tau_S/\tau_R+1)\delta/2$
Fully rough channel	$\begin{cases} \tau_S \ll \tau_R, \\ h \ll \delta, \\ I_x = 0 \end{cases}$	∞	$\delta/2$
Fully rough ZPGBL	$\begin{cases} \tau_S \ll \tau_R, \\ h \ll \delta, \\ f_x = 0 \end{cases}$	∞	$\displaystyle\int_0^\delta \rho x_3(-I_x)/\tau_R \,\mathrm{d}x_3$

Table 2. Examples of l_S and l_R in extreme cases; ZPGBL is short for zero pressure gradient boundary layer.

The values of l_R for a few specific flow scenarios are listed in table 2. Equations (4.6) and (4.9) together give

$$\lambda_p C_R = \frac{2}{Re_{l,R}}\frac{U_\delta}{U_r} + \frac{2}{U_r^2 l_R}\int_0^\delta \left(-\phi\langle\overline{u_1' u_3'}\rangle - \phi\langle\widetilde{\widetilde{u}}_1\widetilde{\widetilde{u}}_3\rangle\right)\mathrm{d}x_3, \tag{4.10}$$

where $Re_{l,R} = U_r l_R/\nu$. Again, the first term represents the laminar contribution and is the only surviving term when the equation is evaluated for laminar flow above a flat plate.

Equations (4.8) and (4.10) provide angular-momentum-based decompositions for the skin friction coefficient C_S and roughness drag coefficient C_R. Just like the kinetic-energy-based decompositions in (4.3) and (4.5), the decompositions in (4.8) and (4.10) fulfil the requirements that we set forth. As before, we have kept the terms that represent internal effects and eliminated the terms that represent external effects. To keep the terms that represent external effects and eliminate the terms that represent internal effects, we need only divide both sides of (4.6) by l, and take l to infinity. The equation again degenerates to the overall force balance.

4.3. *Momentum-based integral*

We multiply the force balance equation with α/δ and subtract it from the mean momentum equation, where α is left undetermined for now. Integrating the resulting equation leads to

$$\begin{aligned}&\left(1-\frac{\alpha}{3}\right)\tau_S/\rho + \left(-\frac{\alpha}{3}\right)\tau_R/\rho \\ &\quad - \int_0^\delta \left(1-\frac{x_3}{\delta}\right)^2 (f_D + \phi f_x - I_x)\,\mathrm{d}x_3 + \left(\frac{\alpha}{3}\right)\left(\int_0^\delta (\phi f_x - I_x)\,\mathrm{d}x_3\right) \\ &\quad = \frac{2\nu U_b}{\delta} + \frac{2}{\delta}\int_0^\delta \left(1-\frac{x_3}{\delta}\right)(-\phi\langle\overline{u_1' u_3'}\rangle - \phi\langle\widetilde{\widetilde{u}}_1\widetilde{\widetilde{u}}_3\rangle)\,\mathrm{d}x_3.\end{aligned} \tag{4.11}$$

The next step is to eliminate terms representing external effects, and isolate the skin friction and drag terms. The following α isolates τ_S:

$$\alpha_S \equiv \alpha = \frac{\displaystyle\int_0^\delta (1 - x_3/\delta)^2 (f_D + \phi f_x - I_x)\,\mathrm{d}x_3}{(1/3)\displaystyle\int_0^\delta (f_D + \phi f_x - I_x)\,\mathrm{d}x_3} = \frac{3}{\tau_S/\rho}\int_0^\delta (1 - x_3/\delta)^2 (f_D + \phi f_x - I_x)\,\mathrm{d}x_3. \tag{4.12}$$

The resulting decomposition of the skin friction coefficient C_S is

$$(0.5U_r^2)C_S = \frac{1}{1 - \alpha_S/3}\left(2\nu\,\frac{U_b}{\delta} + \frac{2}{\delta}\int_0^\delta \left(1 - \frac{x_3}{\delta}\right)(-\phi\langle\overline{u_1' u_3'}\rangle - \phi\langle\widetilde{\widetilde{u}}_1\widetilde{\widetilde{u}}_3\rangle)\,\mathrm{d}x_3\right), \tag{4.13}$$

where the first term on the right-hand side is the only term surviving when the decomposition is evaluated for laminar flow above flat plates.

Similarly, we can isolate τ_R by choosing the following α:

$$\alpha_R \equiv \alpha = \frac{\displaystyle\int_0^\delta (1 - x_3/\delta)^2 (f_D + \phi f_x - I_x)\,\mathrm{d}x_3 - \tau_S/\rho}{(1/3)\left(\displaystyle\int_0^\delta (\phi f_x - I_x)\,\mathrm{d}x_3 - \tau_S/\rho\right)} = \frac{3}{\tau_R/\rho}\left(\int_0^\delta (1 - x_3/\delta)^2 (f_D + \phi f_x - I_x)\,\mathrm{d}x_3 - \tau_S/\rho\right). \tag{4.14}$$

The resulting decomposition of the roughness drag coefficient C_R is

$$(0.5U_r^2)\lambda_p C_R = \left(-\frac{3}{\alpha_R}\right)\left(2\nu\,\frac{U_b}{\delta} + \frac{2}{\delta}\int_0^\delta \left(1 - \frac{x_3}{\delta}\right)(-\phi\langle\overline{u_1' u_3'}\rangle - \phi\langle\widetilde{\widetilde{u}}_1\widetilde{\widetilde{u}}_3\rangle)\,\mathrm{d}x_3\right), \tag{4.15}$$

where U_r is the reference velocity.

The values of α_S and α_R for some specific flow scenarios are tabulated in table 3 and are not elaborated here for brevity. Equations (4.13) and (4.15) give momentum-based decompositions of C_S and C_R, and they satisfy the requirements that we set forth. Again, if we were to keep the terms that represent external effects and eliminate terms that represent internal effects, then we would end up with the overall force balance.

As a final remark for this section, we note that the integrals obtained here should be viewed as alternatives to the existing ones in Fukagata *et al.* (2002), Nikora *et al.* (2019), Renard & Deck (2016) and Elnahhas & Johnson (2022), and provide useful extensions of the integral methods to the rough-wall flows.

5. The DNS details

We provide detailed information about the DNS data (Zhang *et al.* 2023) to which we apply our decompositions. The flow configuration is depicted schematically in figure 2, representing a half-channel with periodicity in the two horizontal directions. The flow

Flow scenario		α_S	α_R
Plane channel	$\begin{cases}\tau_S \gg \tau_R,\\ f_x \gg I_x\end{cases}$	1	$-\infty$
Plane ZPGBL	$\begin{cases}\tau_S \gg \tau_R,\\ f_x \ll I_x\end{cases}$	$\displaystyle\int_0^\delta \frac{\left(1-\frac{x_3}{\delta}\right)^2(-I_x)}{(1/3)\tau_S/\rho}\,\mathrm{d}x_3$	$-\infty$
Transitional rough channel	$\begin{cases}\tau_S \sim \tau_R,\\ h \ll \delta,\\ f_x \gg I_x\end{cases}$	$1-2\tau_R/\tau_S$	$-2-2\tau_S/\tau_R$
Fully rough channel	$\begin{cases}\tau_S \ll \tau_R,\\ h \ll \delta,\\ f_x \gg I_x\end{cases}$	$-\infty$	-2
Fully rough ZPGBL	$\begin{cases}\tau_S \ll \tau_R,\\ h \ll \delta,\\ f_x \ll I_x\end{cases}$	$-\infty$	$\displaystyle\int_0^\delta \frac{\left(1-\frac{x_3}{\delta}\right)^2(-I_x)}{(1/3)\tau_R/\rho}\,\mathrm{d}x_3$

Table 3. Examples of α_S and α_R in extreme cases; ZPGBL is short for zero pressure gradient boundary layer.

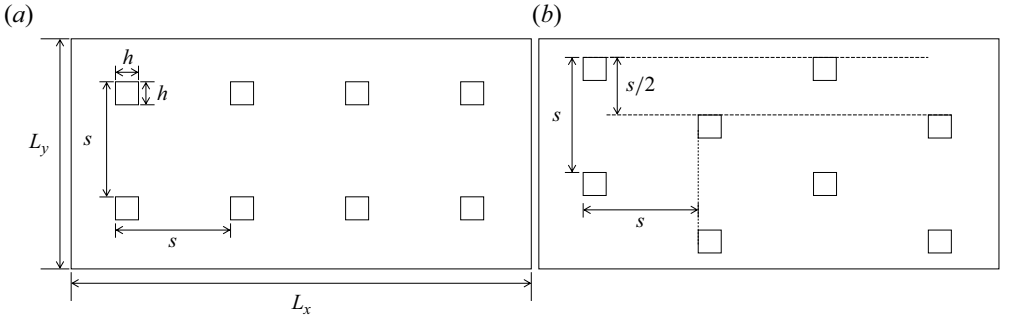

Figure 3. Schematic of the (*a*) aligned and (*b*) staggered arrangements of roughness arrays. The flow is from left to right.

is driven by a constant pressure gradient in the streamwise direction, while the bottom wall is characterized by roughness elements in the form of cubes. The domain height is six times that of the cubes, and we vary the surface coverage density λ_p from 0.11 % to 11.1 %. Additionally, we explore different arrangements of the cubes, including aligned and staggered arrangements, illustrated in figures 3(*a*,*b*), respectively. The friction Reynolds number of the flow is $Re_\tau = u_\tau L_z/\nu = 360$, where $u_\tau = \sqrt{\tau_w/\rho}$ denotes the friction velocity (τ_w is the total rough-wall drag per unit planar area), $L_z(=\delta)$ is the height of the open channel, and ν represents the fluid viscosity.

Our DNS are conducted using the pseudo-spectral code LESGO, which solves the incompressible Navier–Stokes equations utilizing the fractional-step method with a second-order Adams–Bashforth scheme for time marching. Horizontal directions employ a Fourier spectral discretization, and the wall-normal direction uses a second-order staggered-grid finite difference scheme. The immersed boundary method is employed to resolve the roughness elements (Chester, Meneveau & Parlange 2007). This code has

Case	Re_τ	λ_p	s/h	$n_x \times n_y$	Configuration	$L_x/h \times L_y/h \times L_z/h$	$N_x \times N_y \times N_z$
A03	360	11.1 %	3	14 × 7	Aligned	42 × 21 × 6	672 × 336 × 160
A04	360	6.25 %	4	10 × 5	Aligned	40 × 20 × 6	640 × 320 × 160
A05	360	4.00 %	5	8 × 4	Aligned	40 × 20 × 6	640 × 320 × 160
A06	360	2.78 %	6	7 × 4	Aligned	42 × 24 × 6	672 × 384 × 160
A08	360	1.56 %	8	5 × 3	Aligned	40 × 24 × 6	640 × 384 × 160
A10	360	1.00 %	10	4 × 2	Aligned	40 × 20 × 6	640 × 320 × 160
A15	360	0.44 %	15	3 × 2	Aligned	45 × 30 × 6	720 × 480 × 160
A20	360	0.25 %	20	2 × 2	Aligned	40 × 40 × 6	640 × 640 × 160
A25	360	0.16 %	25	2 × 2	Aligned	50 × 50 × 6	800 × 800 × 160
A30	360	0.11 %	30	2 × 2	Aligned	60 × 60 × 6	960 × 960 × 160
S03	360	11.1 %	3	14 × 7	Staggered	42 × 21 × 6	672 × 336 × 160
S04	360	6.25 %	4	10 × 5	Staggered	40 × 20 × 6	640 × 320 × 160
S05	360	4.00 %	5	8 × 4	Staggered	40 × 20 × 6	640 × 320 × 160
S06	360	2.78 %	6	8 × 4	Staggered	48 × 24 × 6	768 × 384 × 160
S08	360	1.56 %	8	6 × 3	Staggered	48 × 24 × 6	768 × 384 × 160
S10	360	1.00 %	10	4 × 2	Staggered	40 × 20 × 6	640 × 320 × 160
S15	360	0.44 %	15	4 × 2	Staggered	60 × 30 × 6	960 × 480 × 160
S20	360	0.25 %	20	2 × 2	Staggered	40 × 40 × 6	640 × 640 × 160
S25	360	0.16 %	25	2 × 2	Staggered	50 × 50 × 6	800 × 800 × 160
S30	360	0.11 %	30	2 × 2	Staggered	60 × 60 × 6	960 × 960 × 160

Table 4. The DNS details: Re_τ is the friction Reynolds number, λ_p is surface coverage density, s is the spacing between two neighbouring roughness elements, h is roughness height, n_x and n_y are the roughness element numbers in the streamwise and spanwise directions, L_x, L_y and L_z are the domain sizes in the streamwise, spanwise and wall-normal directions, respectively, and N_x, N_y and N_z are the grid numbers in the corresponding directions.

been utilized extensively in simulating turbulent flows over rough surfaces (Graham & Meneveau 2012; Cheng & Porté-Agel 2015; Giometto *et al.* 2016; Zhu & Anderson 2018; Yang *et al.* 2019; Zhang *et al.* 2022), and we omit further details here for the sake of brevity.

Table 4 provides additional specifics of the DNS, including domain sizes, grid sizes, roughness arrangements, distance between neighbouring cubes, and surface coverage density. The cases are named based on the [Configuration][Spacing] format, where 'Configuration' is denoted by A or S, and 'Spacing' ranges from 03 to 30. We chose the streamwise and spanwise domain sizes L_x and L_y to be such that $L_x > 2\pi L_z$ and $L_y > \pi L_z$, following Lozano-Durán & Jiménez (2014) and Sharma & Garcia-Mayoral (2020). The grid is uniform in the x and y directions, but stretched in the z direction. The grid resolution satisfies $\Delta x^+ = \Delta y^+ = 3.75$, with $\Delta z^+_{min} < 0.5$ at the wall, and $\Delta z^+_{max} \approx 3$ at the top of the open channel. The grid resolution is comparable to or finer than that used in the existing literature (Kim, Moin & Moser 1987; Lee, Sung & Krogstad 2011; Lozano-Durán & Jiménez 2014; Xu *et al.* 2021). While a finer grid resolution may be necessary for high-order statistics (Yang & Griffin 2021; Chen *et al.* 2023), our current focus is on low-order statistics.

6. Results

6.1. *Drag coefficients*

Figure 4 presents the variation of the bottom-wall friction coefficient C_S and the element drag coefficient C_R with respect to the surface coverage density λ_p. For $\lambda_p \lesssim 1\,\%$, the

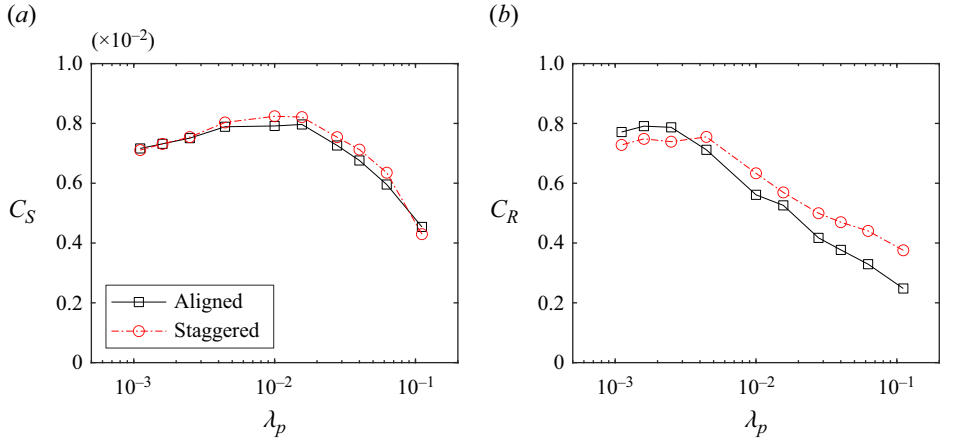

Figure 4. Drag coefficients as functions of the roughness surface coverage density λ_p: (*a*) surface skin friction coefficient C_S; (*b*) element drag coefficient C_R. The black squares with solid lines represent the aligned arrangement, and the red circles with dash-dotted lines represent the staggered arrangement.

bottom viscous friction coefficient C_S increases with λ_p, while for $\lambda_p \gtrsim 1\,\%$, C_S decreases with increasing λ_p. The increase in C_S when λ_p is low is attributed to secondary flows that transport high-momentum fluid from the bulk to the wall layer (Yang *et al.* 2019). These secondary flows manifest as vortex pairs, arising due to the spanwise heterogeneity in surface roughness (Anderson *et al.* 2015). Conversely, the decrease in C_S when λ_p is high is linked to flow sheltering (Raupach 1992), where an upstream roughness element reduces the incoming flow to a downstream roughness, thereby resulting in reduced drag on the downstream roughness. As for the element drag coefficient, C_R remains insensitive to λ_p for $\lambda_p \lesssim 0.4\,\%$, in which range the roughness elements behave as if they are isolated. However, when $\lambda_p \gtrsim 0.4\,\%$, the element drag coefficient starts decreasing with λ_p due to the interactions between the roughness elements that lead to mutual flow sheltering. In this regime, the roughness elements influence one another, resulting in the decrease of C_R with increasing λ_p. Furthermore, it is worth noting that the staggered arrangement consistently yields larger values of C_R compared to the aligned arrangement for $\lambda_p \gtrsim 0.4\,\%$. This is attributed to reduced flow sheltering in rough-wall boundary layers with the staggered roughness arrangement compared to the aligned roughness arrangement (Cheng *et al.* 2007; Hagishima *et al.* 2009; Leonardi & Castro 2010; Yang *et al.* 2016).

6.2. *Kinetic-energy-based decomposition*

In this subsection and the following two subsections, we apply the decompositions to the rough-wall open channel DNS data presented in § 5. We plot against λ_p, but the plots here reflect the effect of decreasing porosity as well.

Figure 5 shows $U_{w,S}/U_b$ and $U_{w,R}/U_b$, where $U_{w,S}$ approaches U_b and large multiples of U_b as λ_p approach 0, i.e. the smooth-wall limit and the fully rough-wall limit, which is consistent with table 1. On the other hand, $U_{w,R}$ approaches large multiples of U_b and U_b as λ_p approach the smooth-wall and fully rough-wall limits, in accordance with table 1. Here, we explain the trends in figure 5. Equation (4.3) is an energy equation. The left-hand side, $U_{w,S}\tau_S$, represents the work done by the bottom-wall viscous friction. It balances the energy loss due to terms on the right-hand side. When λ_p is large, τ_S is small, and $U_{w,S}$ must be large to balance the terms on the right-hand side. Similarly, (4.5) is also an

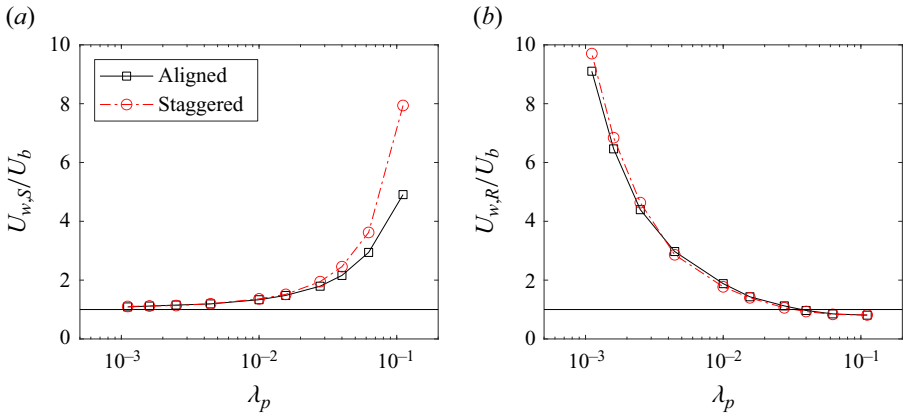

Figure 5. The wall velocity (*a*) $U_{w,S}$ as defined in (4.2), (*b*) $U_{w,R}$ as defined in (4.4). The black squares with solid lines represent the aligned arrangement, and the red circles with dash-dotted lines represent the staggered arrangement. The horizontal line is at $U_w/U_b = 1$.

energy equation. The left-hand side, $U_{w,R}\tau_R$, is the energy source that balances the energy loss on the right-hand side. As λ_p approaches 0, τ_R is small and $U_{w,R}$ must be large. The staggered arrangement leads to a drag partition that is more biased towards the roughness drag, resulting in a larger $(\tau_R + \tau_S)/\tau_S$ than the aligned arrangement in the fully rough limit, which subsequently leads to a larger $U_{w,S}/U_b$ than the aligned arrangement, as per table 1.

Figure 6 shows the decompositions of the wall friction coefficient and the element drag coefficient, i.e. (4.3) and (4.5). Here, we define the C_S components as

$$\left.\begin{aligned} C_{S,V} &= \frac{1}{0.5U_{w,S}U_b^2}\int_0^\delta \nu\left(\frac{\partial\phi\bar{u}_1}{\partial x_3}\right)^2 \mathrm{d}x_3,\\ C_{S,T} &= \frac{1}{0.5U_{w,S}U_b^2}\int_0^\delta \phi\langle\overline{u_1'u_3'}\rangle\frac{\partial\phi\bar{u}_1}{\partial x_3}\,\mathrm{d}x_3,\\ C_{S,D} &= \frac{1}{0.5U_{w,S}U_b^2}\int_0^\delta \phi\langle\widetilde{\bar{u}}_1\widetilde{\bar{u}}_3\rangle\frac{\partial\phi\bar{u}_1}{\partial x_3}\,\mathrm{d}x_3, \end{aligned}\right\} \tag{6.1}$$

which are the contributions from the viscous term, the turbulent production and the wake production, respectively. The C_R components ($C_{R,V}$, $C_{R,T}$, $C_{R,D}$) are defined in a similar way as in (7.1*a–c*) by replacing $U_{w,S}$ with $U_{w,R}$. We make the following observations. First, the wake production is small in both C_S and C_R for the range of λ_p investigated here; at small λ_p, turbulent production and mean flow dissipation are comparable; as λ_p increases, turbulent production becomes the dominant term. Second, we can attribute the increase in C_S as a function of λ_p when λ_p is small in figure 4 to the increase in turbulent production. Considering that this increase in C_S is a result of secondary flows (Yang *et al.* 2019), we may conclude that the presence of secondary flows increases the turbulent production, which in turn increases C_S. Third, the decrease in C_S as a function of λ_p when λ_p is large in figure 4 can be attributed to the decline of both mean flow dissipation and turbulent production with increasing λ_p. Considering that this decrease in C_s is due to flow sheltering, we may conclude that flow sheltering reduces the mean flow dissipation and turbulent production, which in turn reduces C_S. Fourth, flow sheltering also

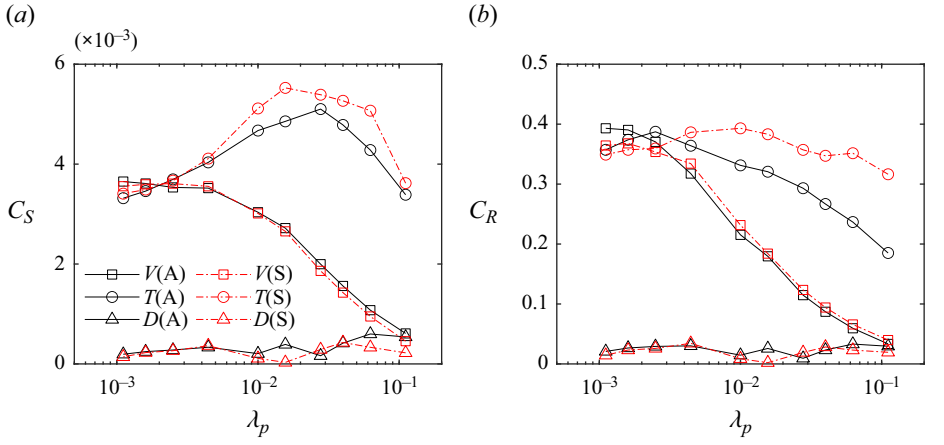

Figure 6. Kinetic-energy-based decomposition of drag coefficient: (*a*) the wall skin friction coefficient C_S per (4.3); (*b*) the element drag coefficient C_R per (4.5). The decompositions contain contributions from the viscous dissipation (squares, denoted as V in the figure), the turbulent production (circles, denoted as T in the figure), and the wake production (triangles, denoted as D in the figure). The black symbols with solid lines are for aligned (A) cube arrays, and the red symbols with dash-dotted lines are for staggered (S) cube arrays.

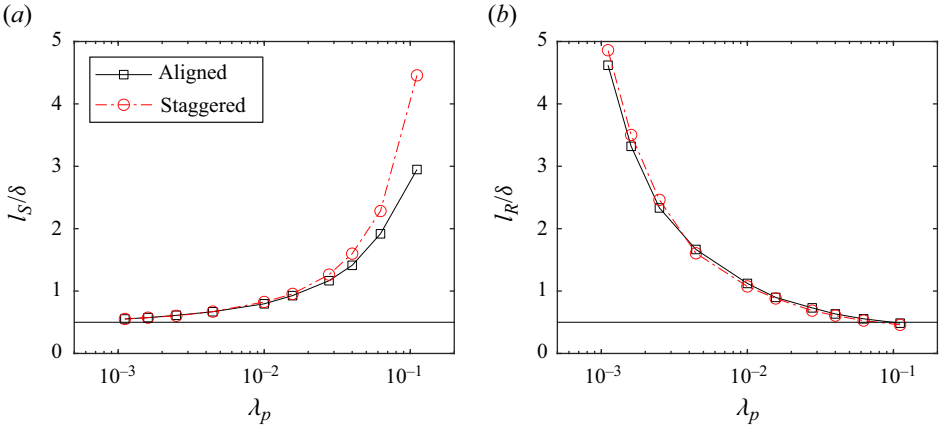

Figure 7. The location of the rotation axis (*a*) l_S as defined in (4.7), and (*b*) l_R as defined (4.9). The horizontal lines are at $l/\delta = 0.5$.

impacts C_R: it leads to reduced turbulent production and mean flow dissipation, which in turn results in a decrease of C_R. Finally, the roughness arrangement affects the turbulent production term at relatively large λ_p values only. At low λ_p values, roughness elements do not interact with each other, and the roughness arrangement does not have an impact on the result. When λ_p is high, the aligned arrangement incurs more flow sheltering than the staggered arrangement, resulting in a more pronounced decrease in turbulent production as a function of λ_p than the staggered arrangement.

6.3. *Angular-momentum-based decomposition*

Figure 7 shows l_S and l_R as in (4.7) and (4.9). Here, l_S approaches 0.5δ and large multiples of 0.5δ at the smooth-wall limit and the fully rough-wall limit, consistent with our analysis of (4.7) as per table 2; l_R, on the other hand, approaches large multiples of 0.5δ and 0.5δ itself at the smooth-wall and the highly rough-wall limit, in accordance

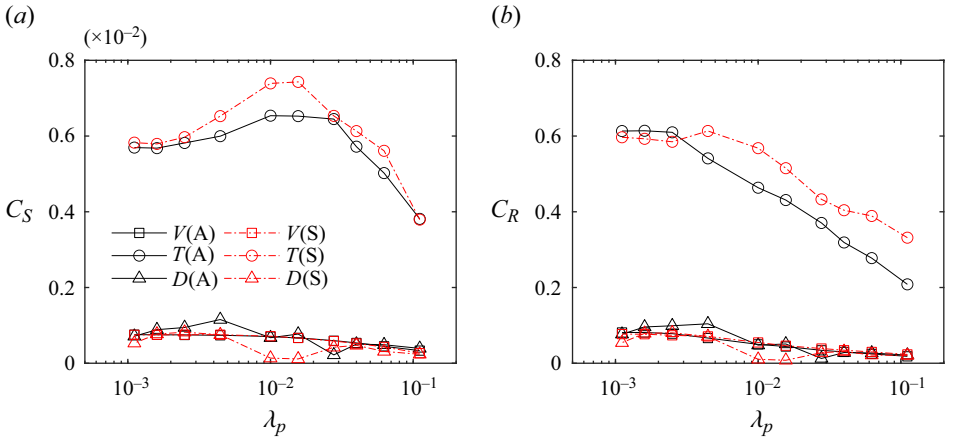

Figure 8. Angular-momentum-based decompositions of (*a*) the wall skin friction coefficient C_S as in (4.8), (*b*) the element drag coefficient C_R as in (4.10). The decompositions contain contributions from the viscous stress (squares), the turbulent stress (circles) and the dispersive stress (triangles). The black symbols with solid lines are for aligned cube arrays, and the red symbols with dash-dotted lines are for staggered cube arrays.

with (4.9) and table 2. Now we explain the trends in figure 7. Equation (4.8) describes the balance of the angular momentum. The left-hand side, $\tau_S l_s/(U_r^2 l_s)$, is balanced by the angular momentum of the stresses on the right-hand side. Hence a large l_S is needed to compensate a small τ_S when λ_p is large. In the smooth-wall limit, the sum of the stress terms equals a linear function of the wall distance, i.e. $\tau_S(1 - x_3/\delta)$, and its integration from $x_3 = 0$ to $x_3 = \delta$ gives $\tau_S\delta/2$. As a result, l_S approaches $\delta/2$ in the smooth-wall limit. A similar analysis applies to l_R and is not repeated here for brevity. Figure 8 shows the decompositions according to (4.8) and (4.10). Compared to the results in figure 6, the results here are less interesting. The turbulent stress is the dominant term in both C_S and C_R, and the contributions due to the viscous stress and dispersive stress are small, at least within the range of surface coverage densities investigated here. Roughness arrangement affects the turbulent stress term and dispersive stress term, with the turbulent stress term generally larger for staggered roughness arrays than for aligned roughness arrays.

6.4. *Momentum-based decomposition*

Figure 9 shows α_S and α_R as defined in (4.12) and (4.14). Here, α_S approaches 1 and a large negative value in the smooth-wall and fully rough-wall limits, consistent with table 3; α_R approaches -2 and a large negative value in the fully rough-wall and smooth-wall limits, also consistent with table 3. The trends in figure 9 can be explained by resorting to the force balance, as in the previous two subsections, where we resorted to the energy and angular momentum equations. Figure 10 shows the decompositions of the skin friction coefficient and the roughness drag coefficient in (4.13) and (4.15). The results are very similar to the results of angular-momentum-based decompositions. The turbulent stress term dominates, with it being larger for staggered arrays than for aligned arrays.

7. Further discussion

The analyses presented in § 6 tell us the processes and their contributions to the skin friction coefficient and the roughness drag coefficient. It has been some 20 years since

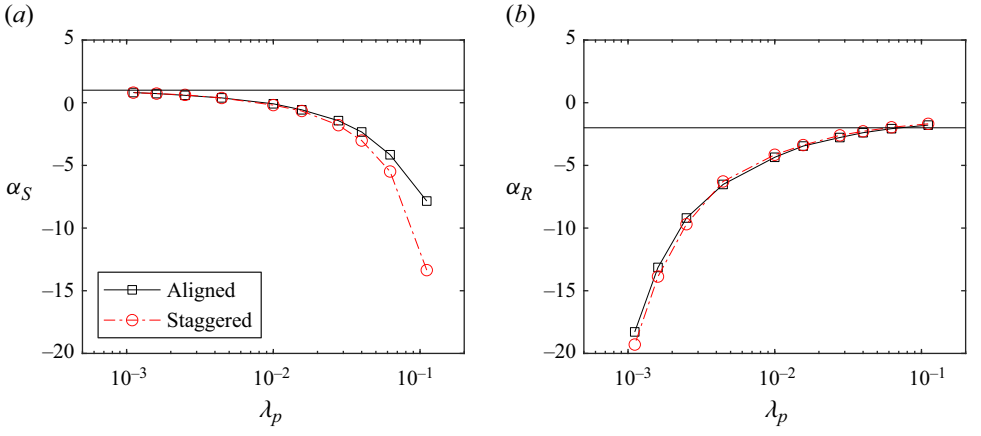

Figure 9. Plots of (*a*) α_S as defined in (4.12), and (*b*) α_R as defined in (4.14). The horizontal lines in (*a*,*b*) are at $\alpha_S = 1$ and $\alpha_R = -2$, respectively.

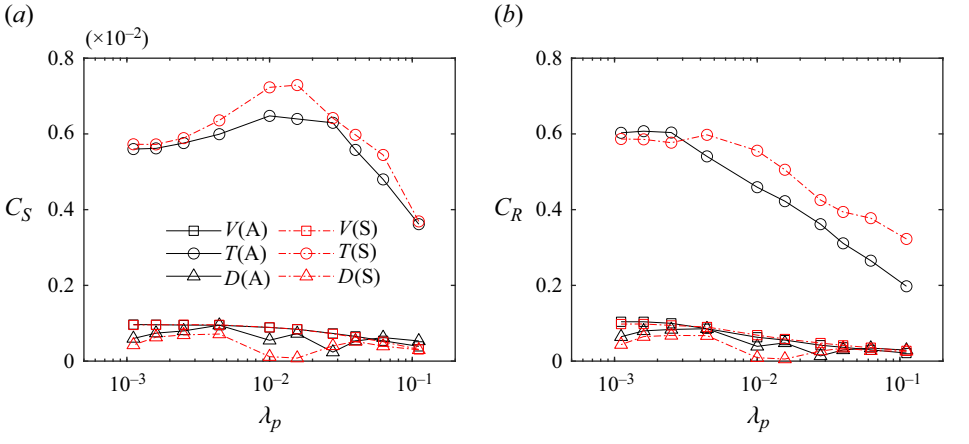

Figure 10. Momentum-based decomposition of (*a*) the wall skin friction coefficient C_S per (4.13), and (*b*) the element drag coefficient C_R per (4.15). The decompositions contain contributions from the viscous stress (squares), the turbulent stress (circles) and the dispersive stress (triangles). The black symbols with solid lines are for aligned cube arrays, and the red symbols with dash-dotted lines are for staggered arrays.

Fukagata *et al.* (2002), and such analyses are somewhat standard. Here we ask: how do eddies at different heights (x_3 locations) contribute to these identified processes, and subsequently to the drag and skin friction coefficients? The same question could be asked about eddies at different x_1 and x_2 locations. For brevity, here we limit the discussion to the kinetic-energy-based decomposition of the skin friction coefficient. It should be clear that the discussion in this section applies equally to the roughness element drag coefficient and other momentum-based, angular-momentum-based decompositions.

Define the viscous dissipation term $\mathcal{D}_{m,S}$, the turbulent production term $\mathcal{P}_{t,S}$ and the wake production term $\mathcal{P}_{d,S}$ as

$$\mathcal{D}_{m,S} = \psi \nu \frac{\partial \bar{u}_1}{\partial x_3} \frac{\partial \phi \langle \bar{u}_1 \rangle}{\partial x_3}, \quad \mathcal{P}_{t,S} = \psi(-\overline{u_1' u_3'}) \frac{\partial \phi \langle \bar{u}_1 \rangle}{\partial x_3}, \quad \mathcal{P}_{d,S} = \psi(-\widetilde{\bar{u}}_1 \widetilde{\bar{u}}_3) \frac{\partial \phi \langle \bar{u}_1 \rangle}{\partial x_3}, \tag{7.1a–c}$$

where $\psi = \delta/(0.5U_{w,S}U_b^2)$. Thus defined terms are functions of the spatial coordinates x_1, x_2 and x_3. Integrating these terms gives the skin friction coefficient per (4.3):

$$C_S = \int_0^1 (\phi\langle\mathcal{D}_{m,S}\rangle + \phi\langle\mathcal{P}_{t,S}\rangle + \phi\langle\mathcal{P}_{d,S}\rangle)\,\mathrm{d}\frac{x_3}{\delta}, \tag{7.2}$$

and the terms $\phi\langle\mathcal{D}_{m,S}\rangle$, $\phi\langle\mathcal{P}_{t,S}\rangle$ and $\phi\langle\mathcal{P}_{d,S}\rangle$, which are functions of x_3, tell us the contributions of the flow at different x_3 locations to the various processes that contribute to C_S.

Figure 11 depicts the viscous dissipation term $\phi\langle\mathcal{D}_{m,S}\rangle$, the turbulent production term $\phi\langle\mathcal{P}_{t,S}\rangle$ and the wake production term $\phi\langle\mathcal{P}_{d,S}\rangle$ as functions of the wall-normal coordinate x_3, for both staggered and aligned cube arrays. When λ_p is small, the viscous dissipation term and the turbulent production term are the dominant terms, which is consistent with the results in figure 6. Both the viscous dissipation term and the turbulent production term have a peak in the viscous layer. This peak and its neighbourhoods represent the majority of the contributions to the two terms. As it is located in the viscous layer, we may conclude that the peak is due to the near-wall cycle and that the skin friction coefficient and the drag coefficient are due to the near-wall cycle when λ_p is small. Eddies due to roughness, on the other hand, do not contribute significantly to the skin friction coefficient C_S. As λ_p increases, the near-wall peak in the viscous dissipation term and the turbulent production term weakens and eventually disappears; meanwhile, a second peak emerges at $x_3 = h$, i.e. the cube height. This second peak can be attributed to the shear layer that forms at the cube height (Raupach, Finnigan & Brunet 1996; Zhang *et al.* 2022). Compared to the first peak in the viscous layer, this second peak is rather narrow and, in the viscous dissipation term, does not compensate for the losses due to the weakening of the near-wall peak. Consequently, the viscous dissipation term decreases as λ_p increases. In contrast, the second peak in the turbulent production term is accompanied by increased contributions from the outer layer, which counter and over-compensate the loss due to the weakening in the near-wall peak. A peak is also found in the wake production term at $x_3 = h$, but the term remains small. Finally, the aligned and staggered arrangements give rise to rather similar distributions of the three terms, with the staggered arrangement leading to a higher and a lower second peak in the turbulent production term and the wake production term, compared to the aligned arrangement.

We may also rewrite (7.2) as

$$C_S = \int_0^{L_x} \langle\mathcal{D}_{m,S}\rangle_{23} + \langle\mathcal{P}_{t,S}\rangle_{23} + \langle\mathcal{P}_{d,S}\rangle_{23}\,\frac{\mathrm{d}x_1}{L_x}, \tag{7.3}$$

where $\langle\cdot\rangle_{23}$ denotes the superficial average (Nikora *et al.* 2013) in the spanwise and wall-normal directions, and $\langle\mathcal{D}_{m,S}\rangle_{23}$, $\langle\mathcal{P}_{t,S}\rangle_{23}$ and $\langle\mathcal{P}_{d,S}\rangle_{23}$ are functions of the x coordinate and tell us how eddies at different x_1 locations contribute to the various process and ultimately to C_S. Figures 12(*a*,*c*,*e*) present $\langle\mathcal{D}_{m,S}\rangle_{23}$, $\langle\mathcal{P}_{t,S}\rangle_{23}$ and $\langle\mathcal{P}_{d,S}\rangle_{23}$ as functions of x_1 for case A20, and figures 12(*b*,*d*,*f*) present the three terms as functions of x_1 for case A05. The two cases correspond to $\lambda_p = 0.11\,\%$ and $11\,\%$. The surface coverage densities of the other cases are in between, and their results are not shown here for brevity. We observe the following. First, the magnitudes of the turbulent production term are found to be similar in cases A05 and A20, but the magnitude of the viscous dissipation term in A05 is notably smaller compared to that in A20. These findings align with those in figure 6. Second, both the viscous dissipation term and the turbulent production term remain approximately constant in the x direction. This constancy implies that the eddies

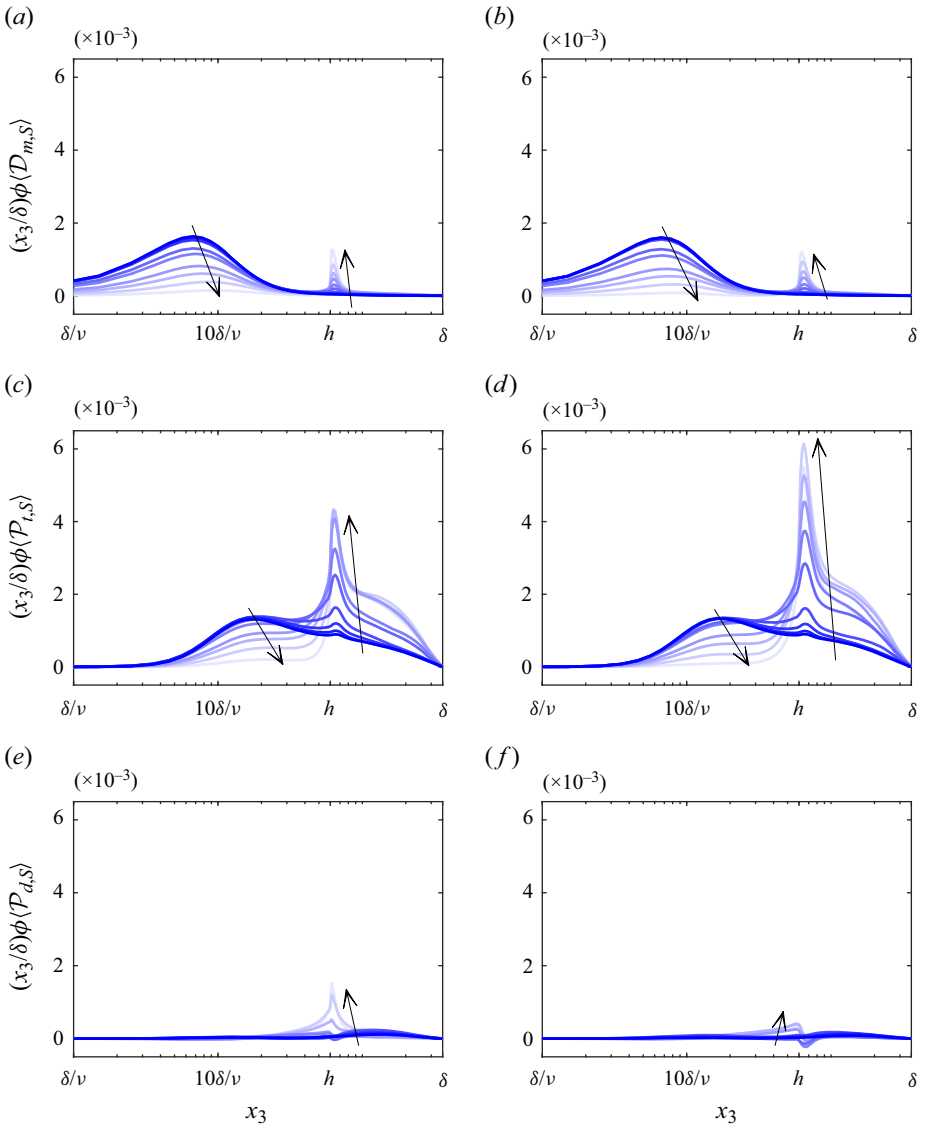

Figure 11. Plots of (a,b) $\phi\langle\mathcal{D}_{m,S}\rangle$, (c,d) $\phi\langle\mathcal{P}_{t,S}\rangle$, (e,f) $\phi\langle\mathcal{P}_{d,S}\rangle$ as defined in (7.1*a–c*) for the (a,c,e) aligned and (b,d,f) staggered cube arrays, with λ_p increasing from 0.11 % (dark blue) to 11 % (light blue). The terms are premultiplied such that the area under a curve represents the integral of the terms. The arrows indicate the direction of increasing λ_p.

contributing to these terms do not exhibit significant variations along the x direction. This piece of information, however, is not very useful since the eddies in this flow are mostly streamwise elongated. Third, the wake production term exhibits considerable variability near the roughness element. Specifically, it contributes negatively to C_S both upstream and downstream of the roughness element.

Finally, we may write (7.2) as

$$C_S = \int_0^{L_y} \langle\mathcal{D}_{m,S}\rangle_{13} + \langle\mathcal{P}_{t,S}\rangle_{13} + \langle\mathcal{P}_{d,S}\rangle_{13}\,\frac{\mathrm{d}x_2}{L_y}, \tag{7.4}$$

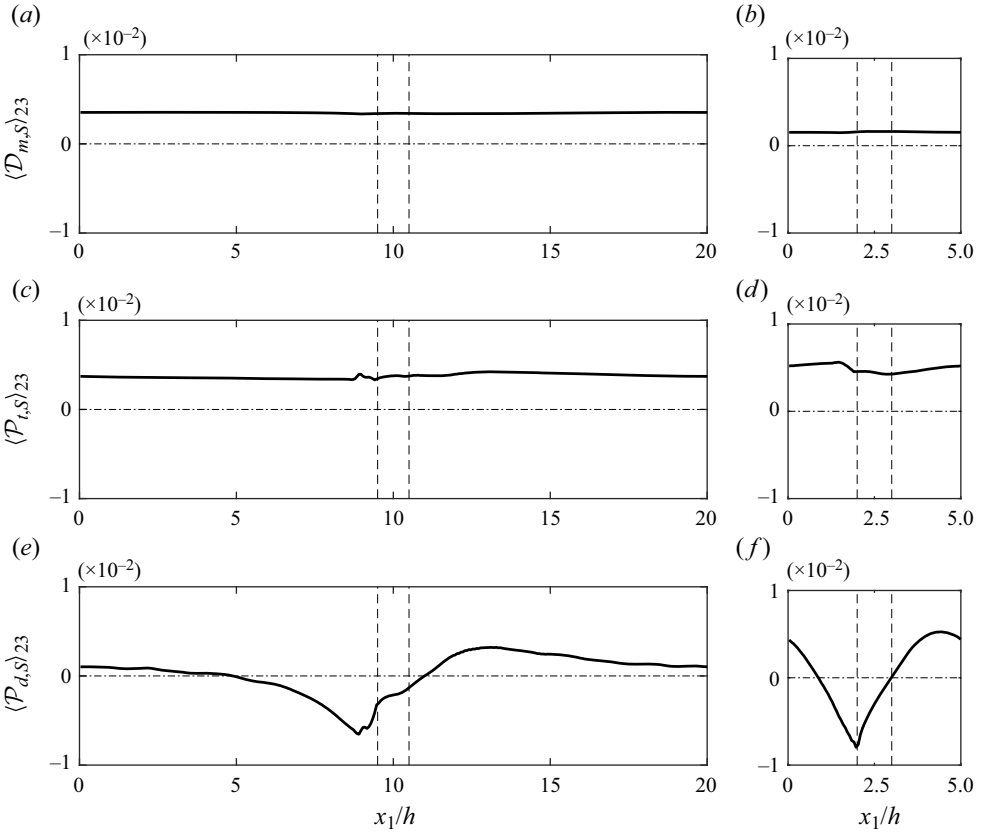

Figure 12. Plots of (*a*,*b*) $\langle \mathcal{D}_{m,S} \rangle_{23}$, (*c*,*d*) $\langle \mathcal{P}_{t,S} \rangle_{23}$, (*e*,*f*) $\langle \mathcal{P}_{d,S} \rangle_{23}$, for (*a*,*c*,*e*) results for A20, and (*b*,*d*,*f*) results for A05. The dashed lines indicate the locations of the cubical roughness. The dash-dotted line is at 0.

where $\langle \cdot \rangle_{13}$ denotes the superficial average in the streamwise and wall-normal directions, and $\langle \mathcal{D}_{m,S} \rangle_{13}$, $\langle \mathcal{P}_{t,S} \rangle_{13}$, and $\langle \mathcal{P}_{d,S} \rangle_{13}$ are functions of the x_2 coordinate and tell us how eddies at different x_2 locations contribute to the various process and ultimately to C_S. Figure 13 shows the three terms as functions of x_2 in A05 and A20. The viscous term is approximately a constant in x_2, with its magnitude reduced from approximately 0.0035 in A20 to 0.001 in A05. The turbulent production term is also approximately constant. The results in figures 13(*a*,*b*) imply that the eddies contributing to the viscous dissipation and turbulent production term are evenly distributed in x_2. Hence secondary flows and horseshoe vortices that wrap around roughness elements, which are present only in the neighbourhood of the surface roughness, cannot contribute significantly to the skin friction coefficient. Regarding the wake production term, we know from figure 6 that the integrated wake production term is small. Nonetheless, the term attains large positive values at the cube location, and large negative values in the neighbourhoods of the roughness element. Taking the result in figure 11 into account, we can conclude that the secondary flows contribute significantly to the wake production term.

The discussion here applies equally to the roughness drag coefficient and angular-momentum-based as well as mean-momentum-based decompositions. These extensions should be straightforward and therefore are not pursued here for brevity.

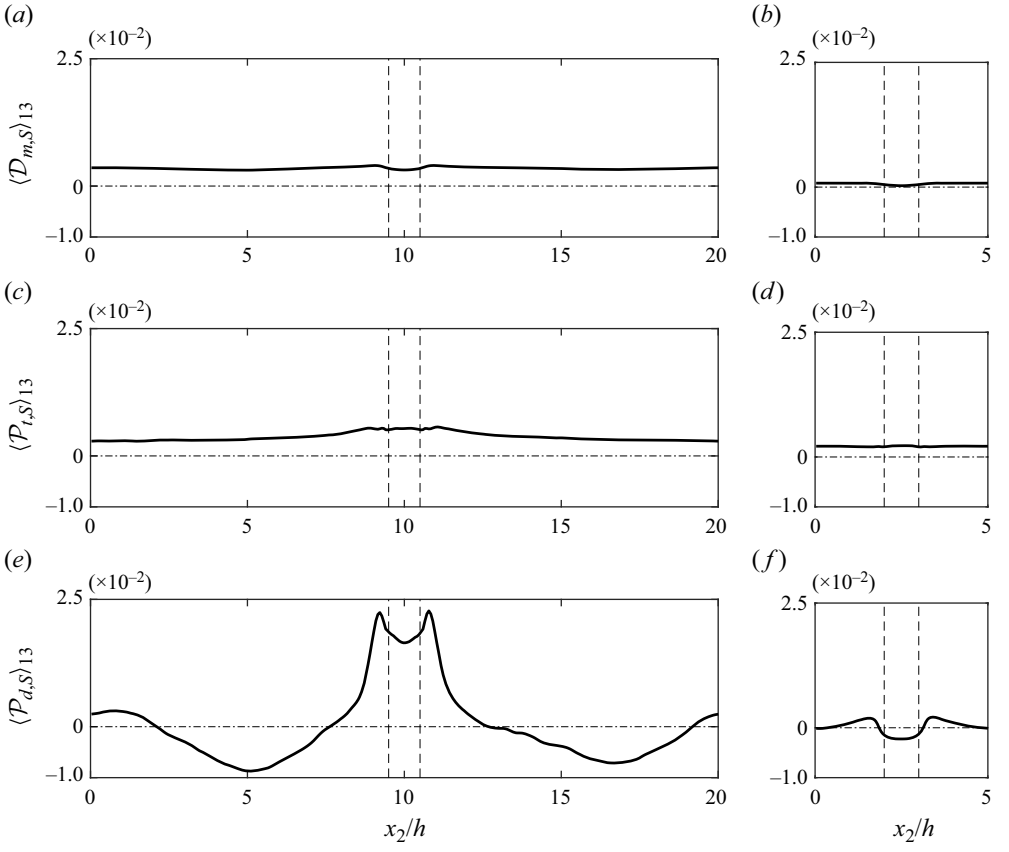

Figure 13. Plots of (*a*,*b*) $\langle \mathcal{D}_{m,S} \rangle_{13}$, (*c*,*d*) $\langle \mathcal{P}_{t,S} \rangle_{13}$, (*e*,*f*) $\langle \mathcal{P}_{d,S} \rangle_{13}$. The dashed lines indicate the locations of the cubical roughness. The dash-dotted line is at 0.

8. Conclusions

We extend the mean momentum equation, the kinetic energy equation, and the angular momentum equation to flow above rough walls. By focusing on effects that are internal to the flow, we obtain separate decompositions for the bottom-wall skin friction coefficient C_S and the roughness drag coefficient C_R, which is a first. These decompositions consistently contain a viscous term, a turbulence term and a roughness term with no free parameters. These terms contain only velocity gradient and velocity fluctuation information, and therefore are Galilean-invariant. The viscous term is the only term when the decompositions are evaluated for laminar-flow and flat-plate scenarios, and the turbulent term is the only term when the decompositions are evaluated for flows at sufficiently high Reynolds numbers and sufficiently small k/δ. In addition, we expand the terms in the decompositions to elucidate the spatial distribution of the various terms in the decompositions.

To demonstrate the applicability of our formulation, we apply the obtained decompositions to DNS data of flow over aligned and staggered cube arrays. The analyses offer insights into the behaviours of C_S and C_R. Take the kinetic-energy-based decompositions as an illustrative example. The analyses show that the viscous dissipation term and the turbulent production term are the dominant terms in the decompositions when the surface coverage density λ_p is small. As λ_p increases, the magnitude of the viscous

dissipation term continuously decreases, while the magnitude of the turbulent production term initially increases and then decreases. Further analyses show that the changes in the viscous dissipation term and the turbulent production term as a function of λ_p are a result of a subdued near-wall cycle and the emergence of a shear layer at the cube height.

Last, but not least, although this paper is limited to the momentum-, kinetic-energy- and angular-momentum-based methods, this reformulation applies to other integrals as well, which is left for future investigation.

Acknowledgements. We thank P. Johnson for constructive comments, and R. Kunz for fruitful discussion.

Funding. W.Z. and M.W. acknowledge the National Science Foundation of China (NSFC; grant nos 12102168, 12225204, 11988102), the Department of Science and Technology of Guangdong Province (grant nos 2023B1212060001, 2020B1212030001) and the Shenzhen Science and Technology Programme (grant no. KQTD20180411143441009) for financial support. X.I.Y. acknowledges NSFC (grant no. 2231037). Numerical simulations have been supported by the Center for Computational Science and Engineering of the Southern University of Science and Technology.

Declaration of interests. The authors report no conflict of interest.

Author ORCIDs.
Wen Zhang https://orcid.org/0000-0002-1181-2018;
Xiang I.A. Yang https://orcid.org/0000-0003-4940-5976;
Minping Wan https://orcid.org/0000-0001-5891-9579.

References

Aghaei-Jouybari, M., Seo, J.-H., Yuan, J., Mittal, R. & Meneveau, C. 2022 Contributions to pressure drag in rough-wall turbulent flows: insights from force partitioning. *Phys. Rev. Fluids* **7** (8), 084602.

Anderson, W., Barros, J.M., Christensen, K.T. & Awasthi, A. 2015 Numerical and experimental study of mechanisms responsible for turbulent secondary flows in boundary layer flows over spanwise heterogeneous roughness. *J. Fluid Mech.* **768**, 316–347.

Bannier, A., Garnier, E. & Sagaut, P. 2015 Riblet flow model based on an extended FIK identity. *Flow Turbul. Combust.* **95**, 351–376.

Chen, P.E.S., Zhu, X., Shi, Y. & Yang, X.I.A. 2023 Quantifying uncertainties in direct-numerical-simulation statistics due to wall-normal numerics and grids. *Phys. Rev. Fluids* **8**, 074602.

Cheng, H., Hayden, P., Robins, A. & Castro, I. 2007 Flow over cube arrays of different packing densities. *J. Wind Engng Ind. Aerodyn.* **95** (8), 715–740.

Cheng, W.-C. & Porté-Agel, F. 2015 Adjustment of turbulent boundary-layer flow to idealized urban surfaces: a large-eddy simulation study. *Boundary-Layer Meteorol.* **155** (2), 249–270.

Chester, S., Meneveau, C. & Parlange, M.B. 2007 Modeling turbulent flow over fractal trees with renormalized numerical simulation. *J. Comput. Phys.* **225**, 427–448.

Chung, D., Hutchins, N., Schultz, M.P. & Flack, K.A. 2021 Predicting the drag of rough surfaces. *Annu. Rev. Fluid Mech.* **53**, 439–471.

Deck, S., Renard, N., Laraufie, R. & Weiss, P.-E. 2014 Large-scale contribution to mean wall shear stress in high-Reynolds-number flat-plate boundary layers up to $Re_\theta = 13\,650$. *J. Fluid Mech.* **743**, 202–248.

Elnahhas, A. & Johnson, P.L. 2022 On the enhancement of boundary layer skin friction by turbulence: an angular momentum approach. *J. Fluid Mech.* **940**, A36.

Fan, Y., Li, W., Atzori, M., Pozuelo, R., Schlatter, P. & Vinuesa, R. 2020 Decomposition of the mean friction drag in adverse-pressure-gradient turbulent boundary layers. *Phys. Rev. Fluids* **5**, 114608.

Flack, K.A. & Schultz, M.P. 2010 Review of hydraulic roughness scales in the fully rough regime. *J. Fluids Engng* **132** (4), 041203.

Fukagata, K., Iwamoto, K. & Hasegawa, Y. 2024 Turbulent drag reduction by streamwise traveling waves of wall-normal forcing. *Annu. Rev. Fluid Mech.* **56**, 45–66.

Fukagata, K., Iwamoto, K. & Kasagi, N. 2002 Contribution of Reynolds stress distribution to the skin friction in wall-bounded flows. *Phys. Fluids* **14** (11), L73–L76.

GAO, A.-K. & WU, J. 2019 A note on the Galilean invariance of aerodynamic force theories in unsteady incompressible flows. *Acta Mechanica Sin.* **35**, 1150–1154.

GIOMETTO, M.G., CHRISTEN, A., MENEVEAU, C., FANG, J., KRAFCZYK, M. & PARLANGE, M.B. 2016 Spatial characteristics of roughness sublayer mean flow and turbulence over a realistic urban surface. *Boundary-Layer Meteorol.* **160** (3), 425–452.

DE GIOVANETTI, M., HWANG, Y. & CHOI, H. 2016 Skin-friction generation by attached eddies in turbulent channel flow. *J. Fluid Mech.* **808**, 511–538.

GOMEZ, T., FLUTET, V. & SAGAUT, P. 2009 Contribution of Reynolds stress distribution to the skin friction in compressible turbulent channel flows. *Phys. Rev.* E **79**, 035301.

GRAHAM, J. & MENEVEAU, C. 2012 Modeling turbulent flow over fractal trees using renormalized numerical simulation: alternate formulations and numerical experiments. *Phys. Fluids* **24** (12), 125105.

HAGISHIMA, A., TANIMOTO, J., NAGAYAMA, K. & MENO, S. 2009 Aerodynamic parameters of regular arrays of rectangular blocks with various geometries. *Boundary-Layer Meteorol.* **132** (2), 315–337.

IWAMOTO, K., FUKAGATA, K., KASAGI, N. & SUZUKI, Y. 2005 Friction drag reduction achievable by near-wall turbulence manipulation at high Reynolds numbers. *Phys. Fluids* **17** (1), 011702.

JIMÉNEZ, J. 2004 Turbulent flows over rough walls. *Annu. Rev. Fluid Mech.* **36**, 173–196.

KIM, J., MOIN, P. & MOSER, R. 1987 Turbulence statistics in fully developed channel flow at low Reynolds number. *J. Fluid Mech.* **177**, 133–166.

LEE, J.H., SUNG, H.J. & KROGSTAD, P.-Å. 2011 Direct numerical simulation of the turbulent boundary layer over a cube-roughened wall. *J. Fluid Mech.* **669**, 397–431.

LEONARDI, S. & CASTRO, I.P. 2010 Channel flow over large cube roughness: a direct numerical simulation study. *J. Fluid Mech.* **651**, 519–539.

LI, W., FAN, Y., MODESTI, D. & CHENG, C. 2019 Decomposition of the mean skin-friction drag in compressible turbulent channel flows. *J. Fluid Mech.* **875**, 101–123.

LOZANO-DURÁN, A. & JIMÉNEZ, J. 2014 Effect of the computational domain on direct simulations of turbulent channels up to $Re_\tau = 4200$. *Phys. Fluids* **26** (1), 011702.

MARUSIC, I., MATHIS, R. & HUTCHINS, N. 2010 High Reynolds number effects in wall turbulence. *Intl J. Heat Fluid Flow* **31** (3), 418–428.

MARUSIC, I. & MONTY, J.P. 2019 Attached eddy model of wall turbulence. *Annu. Rev. Fluid Mech.* **51**, 49–74.

MARXEN, O. & ZAKI, T.A. 2019 Turbulence in intermittent transitional boundary layers and in turbulence spots. *J. Fluid Mech.* **860**, 350–383.

MEHDI, F., JOHANSSON, T.G., WHITE, C.M. & NAUGHTON, J.W. 2014 On determining wall shear stress in spatially developing two-dimensional wall-bounded flows. *Exp. Fluids* **55**, 1656.

NIKORA, V., BALLIO, F., COLEMAN, S. & POKRAJAC, D. 2013 Spatially averaged flows over mobile rough beds: definitions, averaging theorems, and conservation equations. *ASCE J. Hydraul. Engng* **139** (8), 803–811.

NIKORA, V.I., STOESSER, T., CAMERON, S.M., STEWART, M., PAPADOPOULOS, K., OURO, P., MCSHERRY, R., ZAMPIRON, A., MARUSIC, I. & FALCONER, R.A. 2019 Friction factor decomposition for rough-wall flows: theoretical background and application to open-channel flows. *J. Fluid Mech.* **872**, 626–664.

PASSIATORE, D., SCIACOVELLI, L., CINNELLA, P. & PASCAZIO, G. 2021 Finite-rate chemistry effects in turbulent hypersonic boundary layers: a direct numerical simulation study. *Phys. Rev. Fluids* **6**, 054604.

RAUPACH, M.R. 1992 Drag and drag partition on rough surfaces. *Boundary-Layer Meteorol.* **60** (1852), 375–395.

RAUPACH, M.R., FINNIGAN, J.J. & BRUNET, Y. 1996 Coherent eddies and turbulence in vegetation canopies: the mixing-layer analogy. *Boundary-Layer Meteorol.* **25**, 351–382.

RAUPACH, M.R. & SHAW, R.H. 1982 Averaging procedures for flow within vegetation canopies. *Boundary-Layer Meteorol.* **22**, 79–90.

RENARD, N. & DECK, S. 2016 A theoretical decomposition of mean skin friction generation into physical phenomena across the boundary layer. *J. Fluid Mech.* **790**, 339–367.

RICCO, P. & SKOTE, M. 2022 Integral relations for the skin-friction coefficient of canonical flows. *J. Fluid Mech.* **943**, A50.

SCHLICHTING, H. & GERSTEN, K. 2017 *Boundary Layer Theory*, 9th edn. Springer.

SHARMA, A. & GARCIA-MAYORAL, R. 2020 Scaling and dynamics of turbulence over sparse canopies. *J. Fluid Mech.* **888**, A1.

SMITS, A.J., MCKEON, B.J. & MARUSIC, I. 2011 High-Reynolds number wall turbulence. *Annu. Rev. Fluid Mech.* **43** (1), 353–375.

VOLINO, R.J. & SCHULTZ, M.P. 2018 Determination of wall shear stress from mean velocity and Reynolds shear stress profiles. *Phys. Rev. Fluids* **3**, 034606.

WENZEL, C., GIBIS, T. & KLOKER, M. 2022 About the influences of compressibility, heat transfer and pressure gradients in compressible turbulent boundary layers. *J. Fluid Mech.* **930**, A1.

XIA, Z., ZHANG, P. & YANG, X.I.A. 2021 On skin friction in wall-bounded turbulence. *Acta Mechanica Sin.* **37**, 589–598.

XU, D., WANG, J. & CHEN, S. 2022 Skin-friction and heat-transfer decompositions in hypersonic transitional and turbulent boundary layers. *J. Fluid Mech.* **941**, A4.

XU, H.H.A., ALTLAND, S.J., YANG, X.I.A. & KUNZ, R.F. 2021 Flow over closely packed cubical roughness. *J. Fluid Mech.* **920**, A37.

YANG, X. & HOWLAND, M. 2018 Implication of Taylor's hypothesis on measuring flow modulation. *J. Fluid Mech.* **836**, 222–237.

YANG, X.I.A. & GRIFFIN, K.P. 2021 Grid-point and time-step requirements for direct numerical simulation and large-eddy simulation. *Phys. Fluids* **33** (1), 015108.

YANG, X.I.A., SADIQUE, J., MITTAL, R. & MENEVEAU, C. 2016 Exponential roughness layer and analytical model for turbulent boundary layer flow over rectangular-prism roughness elements. *J. Fluid Mech.* **789**, 127–165.

YANG, X.I.A., XU, H.H.A., HUANG, X.L.D. & GE, M.-W. 2019 Drag forces on sparsely packed cube arrays. *J. Fluid Mech.* **880**, 992–1019.

YOON, M., AHN, J., HWANG, J. & SUNG, H.J. 2016 Contribution of velocity–vorticity correlations to the frictional drag in wall-bounded turbulent flows. *Phys. Fluids* **28** (8), 081702.

ZHANG, W., WAN, M., XIA, Z., WANG, J., LU, X. & CHEN, S. 2021 Constrained large-eddy simulation of turbulent flow over rough walls. *Phys. Rev. Fluids* **6**, 044602.

ZHANG, W., YANG, X.I.A., ZHU, X., WAN, M. & CHEN, S. 2023 Asymmetric secondary flows above geometrically symmetric surface roughness. *J. Fluid Mech.* **970**, A15.

ZHANG, W., ZHU, X., YANG, X.I.A. & WAN, M. 2022 Evidence for Raupach *et al.*'s mixing-layer analogy in deep homogeneous urban-canopy flows. *J. Fluid Mech.* **944**, A46.

ZHU, X. & ANDERSON, W. 2018 Turbulent flow over urban-like fractals: prognostic roughness model for unresolved generations. *J. Turbul.* **19** (11–12), 995–1016.